FIRST-PRINCIPLES INVESTIGATION OF NOVEL SINGLE-LAYERS AND HETEROSTRUCTURES OF GROUP III-IV ELEMENTS

A Thesis Submitted to
the Graduate School of
İzmir Institute of Technology
in Partial Fulfillment of the Requirements for the Degree of

MASTER OF SCIENCE

in Chemistry

by
Yankı Öncü YAYAK

January 2022
İZMİR

ACKNOWLEDGMENTS

First of all, I would like to thank my supervisor Assoc. Prof. Dr. Ümit Hakan YILDIZ for sharing his knowledge, advices, and motivations throughout the time of my master's education.

I also would like to express my deepest appreciation to my co-supervisor Prof. Dr. Hasan ŞAHİN for his endless support and teachings.

I very much appreciate my thesis committee members, Prof. Dr. Mustafa EMRULLAHOĞLU, Assoc. Prof. Dr. Engin DURGUN and Assoc. Prof. Dr. Serkan ATEŞ for their valuable time and attandance.

I would like to thank CENT group members, Dr. Mehmet YAĞMURCUKARDEŞ, Dr. Hasan AYDIN, Yiğit SÖZEN, Fırat TAN, Tuna DURAN, Elçin ŞAHİN, Uğur Can TOPKIRAN, Ahmet Kutay ÖZYURT, and Egem Deniz MOLAVALI. It has been a tremendous experience working with you day by day.

I cannot begin to express my thanks to my friends, Tuğçe KÜÇÜKTARTAR, Alper ŞAHİN, Doğacan ERSOY, Beraat Umur KAYA, Emre KARABURUN, Ezgi VURAL, Suay DARTAR and Devrim BULSOY. It was easy coming to school each day knowing you would be there to have coffee breaks, lunch breaks and so much more. I enjoyed every single second I spent with you guys.

Last but not least, my mother, my father, my sister, my grandmother, my aunt and my late uncle, I cannot thank you enough for your love, support, and many other things that words can't describe. You have been there for me no matter what the circumtances were.

ABSTRACT

FIRST-PRINCIPLES INVESTIGATION OF NOVEL SINGLE-LAYERS AND HETEROSTRUCTURES OF GROUP III-IV ELEMENTS

Since the discovery of graphene, two-dimensional materials have been the focus of interest in various branches in scientific community. Wide range of ultra-thin materials have been investigated both theoretically and experimentally such as metal chalcogenides, Xenes and h-BN. In addition to this, two-dimensional (2D) van der Waals heterojunctions have become one of the central research topics due to their wide range of possibilities. Since 2D van der Waals heterostructures are combinations of two or more ultra-thin materials with different properties, creating a heterostructure with desired optical, electrical and/or mechanical property is theoretically probable. Motivated by these, this thesis focus on the investigation of structural, vibrational and electronic properties of 2D materials and their heterostructures by means of density functional theory-based first-principle calculations.

In chapter 3, single-layer Ge_3N_4 is shown to be both electronically and dynamically stable. Also, simulated Raman spectrum of single-layer Ge_3N_4 have characteristic vibrational properties. Another property of single-layer Ge_3N_4 is that it is a indirect band gap semiconductor and this property is uneffected by external strain. And lastly, the value of band gap varies with the applied external strain.

In chapter 4, a dynamically stable single layer structure of AlAs is proposed and four possible stackings of AlAs/InSe heterobilayer were investigated. Electronic band dispersions revealed that all four stackings are direct band gap semiconductors and have type-II alignment. Moreover, simumlated raman spectra revelaed that identification of the 1T and 2H phase can be done with Raman spectroscopy. The band gap can be tuned based on the direction and magnitude of the electric field. Direct to indirect band gap transition as well as heterojunction type changes from type II to type I occurs under negative electric field.

ÖZET

GRUP III VE IV ELEMENTLERİNİN TEK KATMANLI VE HETEROYAPILARININ İLK PRENSİPLER İLE İNCELENMESİ

Grafenin keşfinden bu yana iki boyutlu malzemeler bilim dünyasının çeşitli alanlarının ilgi odağı haline geldi. Geçiş metali kalkojenleri, Xenler, h-BN gibi birçok ultra ince malzeme gerek teorik gerek deneysel olarak incelendi. Bunlara ek olarak, iki boyutlu van der Waals heteroyapıları da sahip oldukları değişik olasılıklardan ötürü araştırmaların merkezinde yer almaktadır. Bu heteroyapılar, iki ve ya daha fazla farklı özellikli ultra ince malzemenin birleşiminden oluştuğu için, istenilen optik, elektronik ve ya mekanik Ãűzelliklere sahip bir heteroyapı oluşturmak teorik olarak mümkün. Bu konulardan motive olarak, bu tezin odağı da iki boyutlu malzemelerin ve heteroyapılarının yapısal, ilk-prensiplere dayalı yoğunluk fonksiyoneli teorisi kullanarak elektronik ve titreşimsel özelliklerinin incelenmesidir.

3. bölüm, tek katmanlı Ge_3N_4 yapısının elektronik ve dinamik olarak kararlı olduğunu gösteriyor. Ayrıca, teorik olarak elde edilmiş Raman spektrumu tek katmanlı Ge_3N_4 kristalinin karakteristik titreşimsel özelliklerini içeriyor. Tek katmanlı Ge_3N_4 bir başka özelliği ise, endirekt yarı-iletken özelliği dışarıdan uygulanan ekstra gerilme kuvvetinden etkilenmemesi. Son olarak band aralığının, uygulanan gerilmenin şiddetine bağlı olarak değiştiği gözlemlenmiştir.

4. bölümde ise, stabil tek katmanlı AlAs kristal yapısı teorik olarak sunulmuş, AlAs ve InSe birleşiminden oluşan olası 4 farklı heteroyapı incelenmiştir. Bu 4 yapının elektronik band dağılımları çıkarıldığında hepsinin II. tip direkt yarı-iletken olduğu bulunmuştur. Dahası, simüle edilmiş Raman spektrumu 4 olası heteroyapının 1T ve 2H fazlarının ayırt edilebildiğini göstermiştir. Son olarak, harici bir elektrik alan etkisinde direkt-endirekt geçişinin yanı sıra, tip-II ve tip-I geçişi elde edilmiştir.

TABLE OF CONTENTS

LIST OF FIGURES

Figure **Page**

Figure **Page**

LIST OF TABLES

Table **Page**

CHAPTER 1

INTRODUCTION

Developing technology requires not only better but also smaller devices to use in smartphones, computers, biosensors robotics and other similar areas. That's why, nanotechnology takes an important place in our daily lives and it most likely will be a key element in the future as well. Nanotechnology deals with materials sized between 1 to 100 nanometers. It processes matters on atomic or molecular scale in order to produce new materials or devices with desired properties. However, scales as low as nanometers are the quantum-realm, thus usual chemical and physical rules are no longer valid. There begin the effects of quantum mechanics. At the two-dimensional (2D) limit, electrons are confined which means they can no longer propagate in three dimensions, and this alters the physical properties of the materials.

Graphene, which is the first 2D material ever isolated, has been at the center of the attention since the day it was obtained from graphite.[1] It consists of sp^2 hybridized C-C bonds and electronic and mechanic properties of graphene made it a promising material for nano applications.[2,3] It is still the thinniest (0.34 nm thickness) and strongest material ever known.[4] Graphene has been widely studied, thus its characteristics are well known. Both experimentally measured and theoretically predicted properties of graphene surpass many other material. For example, room-temperature electron mobility of graphene is 2.5×10^5 $cm^2\ V^{-1}\ s^{-1}$,[5] while theoretical limit is $\sim 2 \times 10^5$ $cm^2\ V^{-1}s^{-1}$.[6] Graphene's thermal conductivity is above 3,000 $W\ mK^{-1}$.[7] Furthermore, Young's modulus of 1 TPa and intrinsic strength of 130 GPa prove its strength.[8] Also, other properties like optical absorption of π $\alpha = 2.3\%$,[9] being impermeable to gases,[10] having the capacity of carrying high electric current densities,[11] and easy functionalization[12,13,14] enhances the magnificence of graphene. Combination of these features of graphene let it find usage in areas such as desalination,[15] healthcare,[16,17] energy storage,[18] drug delivery,[19] solar cells,[20] flexible electronics,[21] and so on. Nevertheless, graphene can only be activated via functionalization due to its almost chemically inert nature.[22] In addition to this, developing technology requires nano-sized materials of different classes like semiconductors, insulators and metals but graphene has

zero band gap and this limits its applications. That's why, graphene-like 2D materials such as transition metal dichalcogenides (TMDs),[23,24,25,26] Xenes,[27,28,29] hexagonal boron nitride (h-BN),[30] etc. are still quite appealing.

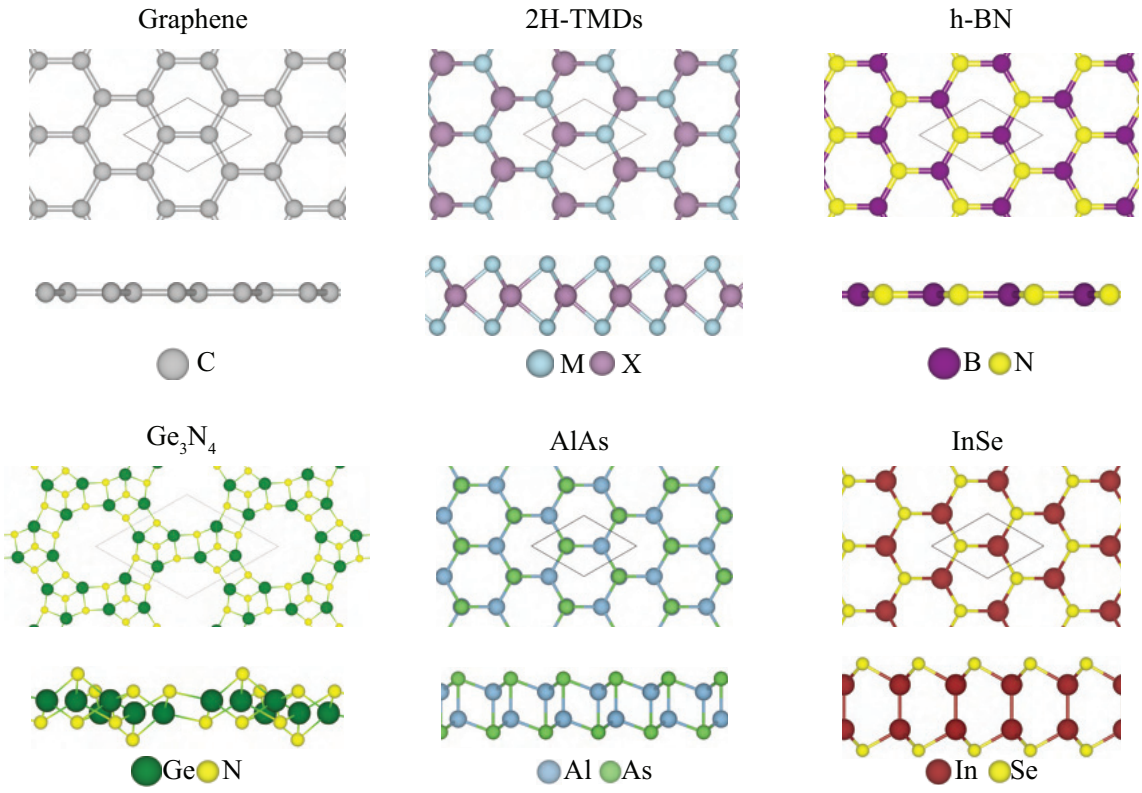

Figure 1.1. Most popular two-dimensional single-layer materials (top) and the ones that are investigated in this thesis (bottom).

Compounds that are formed by at least one chalcogen anion and metal cations are called metal chalcogenides. The expression metal chalcogenide usually refers to molecules consist of sulfur, selenium or tellurium alongside metals, even though all group VIA elements are classified as chalcogens. Besides graphene, metal chalcogenides have appeared as popular 2D materials because of their wide range of applications. These materials can be divided into two subgroups based on their metals: transition metal chalcogenides (TMCs) and main group metal chalcogenides (MMCs). TMCs can also be examined in two different groups. First one is the well-known 2D transition metal dichalcogenides (TMDs), which are in the form of MX_2 (M can be Mo, W, V, Nb, Ta and X can be S, Se, Te). TMDs can either be metallic (M=Nb, Ta)[31,32,33] or semiconductors (M=Mo, W).[23,34,35,36] The interesting properties about semiconductor TMDs are indirect-direct bandgap tran-

sition from bulk to single layer and thickness dependent band gaps which varies from 1.0 to 2.1 eV.[23,24] These properties made TMDs plausible materials in applications like sensors,[37] catalysis,[38] solar cells,[39] photothermal therapy,[40,41] and bioapplications.[42,43] On the other hand, TMTs drew much less attention compared to TMDs, but they might still be used in spintronics, nanoelectronics and nanophotonics.[44,45,46] Besides TMCs, main group metal chalcogenides are also promising materials as they are used in applications such as photovoltaics,[47,48,49] photodetectors,[50,51] sensors,[52] transistors,[53] piezoelectrics[54] and so on.

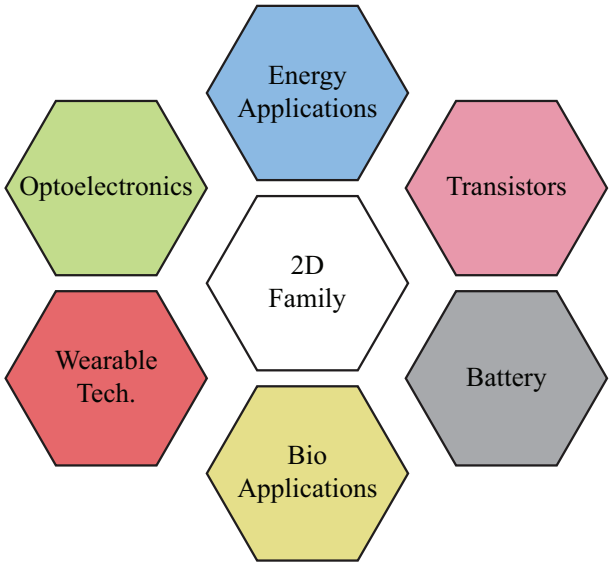

Figure 1.2. Some applications of two-dimensional materials.

Apart from the hunt for new graphene-like 2D structure, heterojunctions consisting of 2D materials have also emerged as a hot research topic.[55,56,57,58,59,60] These heterostructures offer interesting properties and applications because they not only preserve properties of their building blocks, but also introduce new aspects like as high quantum efficiency,[61] high carrier mobility,[62] and tunable optical properties[63] thus making them suitable for nanoelectronics applications.[64,65,66] In other words, van der Waals heterostructures exhibit exciting physical and chemical properties which offers an enormous research area and possibility for device engineering at atomic scale. That's why many 2D ultrathin structures from different material groups are still being searched for the exploration of novel vertical heterostructures.

CHAPTER 2

THEORETICAL BACKGROUND AND METHODOLOGY

As their size gets smaller, systems start to follow quantum mechanical laws instead of Newton's laws. Properties of such systems are stored in their wave function, ψ, and these porperties can be revealed by solving the Schödinger equation,

$$\hat{H}\psi_i = E_i\psi_i \tag{2.1}$$

where $\hat{H}$ is an energy operator called the Hamiltonian operator, E_i refers to the energy eigenvalue of a that quantum state, and ψ_i is the wave function of the energy eigenvalue. The Hamiltonian of a system consists of both potential and kinetic terms of every possible interaction between electrons and nuclei. The Hamiltonian operator when all the terms are added is,

$$\begin{aligned}\hat{H} = &\frac{\hbar}{2m_e}\sum_i \nabla_i^2 - \frac{1}{4\pi\varepsilon_0}\sum_{i,A}\frac{Z_A e^2}{|\boldsymbol{r}_i - \boldsymbol{R}_A|} + \frac{1}{2}\frac{1}{4\pi\varepsilon_0}\sum_{i\neq j}\frac{e^2}{|\boldsymbol{r}_i - \boldsymbol{r}_j|} - \sum_A \frac{\hbar^2}{2M_A}\nabla_A^2 \\ &+ \frac{1}{2}\frac{1}{4\pi\varepsilon_0}\sum_{A\neq B}\frac{Z_A Z_B e^2}{R_A - R_B}\end{aligned} \tag{2.2}$$

where i and j indices stand for electrons, Z_A and Z_B are the nuclear charges, M_A and M_B are the mass of nuclei, **r** and **R** denote to the spatial coordinate of corresponding electron or atom, respectively, m_e is the electron mass, e is the electron charge, $\hbar$ is the Planck constant, and $1/4\pi\epsilon_0$ is the Coulomb constant. The first and the fourth terms refer to the kinetic energy of electrons and nuclei, respectively. The second, third and the last term constitute the potential energy operator, which equal to electron-nucleus, electron-electron, and nucleus-nucleus interactions, respectively. Simple systems such as hydrogen-like systems or sole particles have Hamiltonians that are free of most interaction terms, thus their Schödinger equations are easy to solve. However, it gets messy as the number of interacting particles increase. For systems with large number of electron-electron interactions, it is almost not possible solve the Schödinger equation and various methods are used to obtain approximate solutions.

2.1. Density Functional Theory (DFT)

Density functional theory (DFT) is a popular computational quantum mechanical model that offers first-principles approach to solve the Schödinger equation of many-body systems. It is widely used in chemistry, physics and material science to investigate the various ground-state properties of atoms, molecules and condensed matters. DFT uses functionals of electron density which depend only on x, y and z coordinates. Therefore, the many-body system of N electrons of 3N spatial coordinates is reduced to 3 spatial coordinates. That is why, DFT is computationally cheap and less time consuming along with good accuracy.

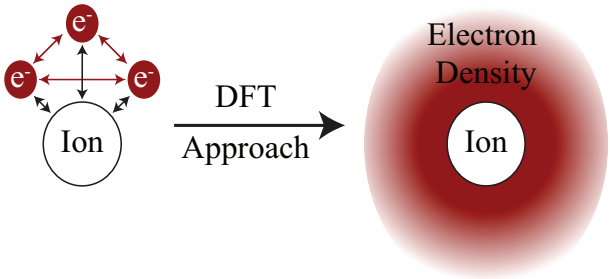

Figure 2.1. Density functional theory approach to a many-body system. Arrows (left) represents the corresponding interactions between electrons and the nuclei.

2.1.1. Hohenberg-Kohn Theorems

Hohenberg-Kohn theorems are the basis of the Density Functional Theory. They say that functionals of electron density can be used to represent the ground state of a many body system.[67] This assumtion is divided into two theories; (i) the external potential energy, V_{ext}, of a many body system is in agreement with a functional of electron density, $n_{(r)}$, that is unique for said system. (ii) The total energy of the system can be obtained by applying the electron density functional as the it results with a global minimum energy value if the ground-state density is given as the input density. The ground-state energy is given by the expectation value of the Hamiltonian,

$$E = \frac{\langle \Psi_0 | H | \Psi_0 \rangle}{\langle \Psi_0 | \Psi_0 \rangle} = T[n] + V_{int}[n] + E_{II} \int d^3\mathbf{r} V_{ext}(\mathbf{r}) n(\mathbf{r})$$
$$T[n] + V_{int}[n] = F_{HK}[n] \tag{2.3}$$

where $T[n]$ is the kinetic energy of electrons, V_{int} is the energy of electron-electron interactions, and E_{II} is the nuclei-nuclei interaction. F_{HK}[n] is a constant which represents to the total kinetic energy of electrons.

2.1.2. Kohn-Sham Equations

Kohn-Sham proposed a method based on Hohenberg-Kohn theorems in which the charge density is divided to all densities containing N electrons to minimize the functional energy. The system can be represented as a many-body system with non-interacting electrons.[68] The ground-state electron density is acquired from the solution of the Schödinger equation of non-interacting terms, while the electron-electron interactions are taken into account with another functional, called exchange-correlation functional, $E_{xc}[n]$. Hence, the functional of the Kohn-Sham method is defined as;

$$E_{KS} = T[n] + \int d^3\mathbf{r} V_{ext}(r) n(r) + E_H[n] + E_{xc}[n] + E_{II}, \tag{2.4}$$

where $E_H[n]$ is called the Hartree energy and given by the following formula,

$$E_H[n] = \frac{e^2}{2} \int d^3\mathbf{r} d^3\mathbf{r}' \frac{n(\mathbf{r}) n(\mathbf{r}')}{|\mathbf{r} - \mathbf{r}'|}. \tag{2.5}$$

The Schrödinger like equation of non-interacting electrons is,

$$\hat{H}_{KS} \Psi_i(r) = \varepsilon_i \Psi_i(r), \tag{2.6}$$

where $\hat{H}_{KS}$ and ε_i are effective Kohn-Sham Hamiltonian and energy eigenvalues, respectively. $\Psi_i(r)$ are the single-particle wave functions or Kohn-Sham orbitals. Spin operators are not taken into account to simplify the equation. Kohn-Sham orbitals and ground-state electron density functional relation is given by,

$$n(\mathbf{r}) = \sum_{i=1}^{N} |\Psi_i|^2, \tag{2.7}$$

and the effective Hamiltonian is,

$$\hat{H}_{KS}(\mathbf{r}) = -\frac{1}{2}\nabla^2 + V_{KS}(\mathbf{r}), \tag{2.8}$$

in which the effective Kohn-Sham effective potential, $V_{KS}(\mathbf{r})$,

$$V_{KS}(\mathbf{r}) = V_{ext}(\mathbf{r}) + V_H(\mathbf{r}) + V_{xc}(\mathbf{r}), \tag{2.9}$$

that is the total of the external, $V_{ext}(\mathbf{r})$ Hartree, $V_H(\mathbf{r})$ and exchange-correlation, $V_{xc}(\mathbf{r})$ potentials, respectively.

As a starting point, inital guess of electron density has to be provided. Then, the effective Kohn-Sham potential, $V_{KS}(\mathbf{r})$ is constructed for the given electron density. After that, iterative solution is carried out in which the results of each iteration is compared to earlier one in order to determine if convergence is reached. Finally, the resulting density is used to obtain the total energy of the system.

2.2. Computational Parameters

In chapter this thesis, structural optimizations and electronic band dispersions were investigated using the first-principles calculations within the density functional theory as implemented in the Vienna Ab initio Simulation Package.[79,80] The Plane-wave projector-augmented wave potentials were used and the exchange-correlation potential was approximated using the Perdew-Burke-Ernzerhof (PBE) form of the generalized gradient approximation (GGA).[81]

In the chapter 3, 520 eV was taken for the energy cutoff value and the kinetic energy cutoff and 10^{-5} eV was set as the the convergence criterion. In order to include include The van der Waals (vdW) interaction, DFT-D2 method of Grimme.[82] was used. Charge transfer between atoms was determined with Bader method. To eliminate the interactions with adjacent cells, 15 Å vacuum spacing was selected along the z-axis. For the structural optimization of the primitive unit cell, a $5\times5\times1$ k-point mesh was applied for structural optimization of unit cell, while for more accurate density of states calculations it was doubled. Since GGA underestimates the band gap, better assumption of electronic properties was calculated with The Heyd-Scuseria-Ernzerhof (HSE06) functional.[83] The

cohesive energy per atom was obtained with the given formula;

$$E_{Coh} = \frac{n_{Ge}E_{Ge} + n_N E_N - E_{sys}}{n_{tot}} \tag{2.10}$$

where n_{Ge} and n_N are the number of Ge and N atoms per unit cell, respectively. n_{tot} refers to the total number of atoms per unit cell, while energies of single Ge and N atom are given by E_{Ge} and E_N, respectively. PHON code was applied to calculate the vibrational properties. Simulated STM images were obtained with the following formula by calculating partial charge densities of the primitive unit cell in the range [-3,0] eV;

$$E_{total} = \sum_{n}^{h} E_n e^{-kz_n} \tag{2.11}$$

where E_{total} refers the summation of charge density matrix, n is the number of layer, h is the height (thickness) of the structure, E_n corresponds to the partial charge density matrix for the n^{th} layer, while k is a constant, and z_n is the tip distance of the simulated STM in z-axis.

In chapter 4, The Becke-Johnson damping of the DFT-D3 method was used to implement the van der Waals (vdW) corrections.[82] For more accurate electronic band gap calculations, Heyd-Scuseria-Ernzerhof (HSE06) within spin-orbit coupling (SOC) was taken into account. The plane-wave functions were expanded up to a 500 eV of kinetic energy cutoff in the while the criterion for total energy convergence was taken to be 10^6 eV with the corresponding convergence of the forces to be less than 10^{-5} eV/Å. 20 Å of vacuum spacing was introduced in order to prevent interactions between repeating structures along the out-of-plane direction. During the ionic relaxations, the Brillouin Zone (BZ) of the unit cell was sampled using (18×18×1) k-points. The layer-layer interaction energy was calculated by using the formula; E_{int} = E_{InSe} + E_{AlAs} - E_{het}, where E_{InSe}, E_{AlAs}, and E_{het} stand for the total energies of single layers of InSe and AlAs, and for InSe/AlAs heterostructure, respectively. For the calculation Raman spectra, the zone-centered vibrational modes were calculated using small-displacement methodology. The corresponding Raman activity of each phonon mode was obtained through the derivative of the macroscopic dielectric tensor using the finite-difference method.

CHAPTER 3

FIRST-PRINCIPLES INVESTIGATION OF STRUCTURAL, RAMAN AND ELECTRONIC CHARACTERISTICS OF SINGLE LAYER Ge_3N_4

Group-IV nitrides have drawn attention because of their easy accessibility, low-cost preparation, chemical stability and electrically tunability. Germanium nitride (Ge_3N_4), a member of group-IV nitrides, has been widely studied for a long time and was first experimentally realized by reacting metallic germanium and ammonia gas at high temperatures in 1930.[135] After that, various experimental methods have been developed in order to synthesize different phases of Ge_3N_4.[136,137,138,139,140] While the cubic phase of Ge_3N_4 was synthesized using laser-heated diamond anvil cell[137], its γ-phase was demonstrated by controlling the pressure and temperature in α- and β-phases.[138]

The electronic and optical properties of the synthesized phases of bulk Ge_3N_4, which are large-gap semiconductors, have been studied by means of theoretical simulations.[141,142,143,144,145,146] Molina et al. investigated the properties of five different phases of Ge_3N_4 and β-Ge_3N_4 was reported to be the most stable phase among them.[141] Spinel germanium nitrides can be considered as multifunctional materials with their large exciton binding energies and tunable band gaps.[145] Among α-, β-, and γ-Ge_3N_4 phases, the β-Ge_3N_4 was reported to be a direct band gap semiconductor.[146] In addition, the thermal conductivity of γ-Si_3N_4 and γ-Ge_3N_4 were studied by comparing to that of β-Si_3N_4 and it was shown that both γ-Si_3N_4 and γ-Ge_3N_4 exhibit higher thermal conductivity at room temperature with less anisotropy.[147] In another study, both experimental and computational methods were used in order to investigate the potential of group-IV nitrides as optoelectronic materials and it was found that the Ge_3N_4 has lower electron effective masses compared to that of γ-Si_3N_4.[148,149,150,151,152] Moreover, Maeda et al. reported that ultrathin Ge_3N_4 was used to create Ag/Ge_3N_4/Ge metal-insulator-semiconductor device that exhibits capacitance-voltage characteristics with no hysteresis.[149] The properties of Au/Ge_3N_4/Ge capacitors were also studied and it was found that the gate leakage current density is lower compared to that of poly-Si/SiO_2/Si while being thermally stable at higher

temperatures.[150] Other applications of Ge_3N_4 includes solar cell design and photocatalyst in water splitting process. It was also proposed that adsorption of RuO_2 to β-Ge_3N_4 surface created a non-oxide photocatalysts for overall water splitting as oxygen evolution reaction occurs on the surface of β-Ge_3N_4 whereas hydrogen evolution reaction tends to occur on RuO_2.[153] Enhancement by ammonia treatment of the photocatalytic activity of β-Ge_3N_4 in water splitting process was reported.[154] Recently, a solar cell design was proposed where spinel Ge_3N_4 and Si_3N_4 were used as solar cell absorber materials.[155]

In this work, two-dimensional form of Ge_3N_4 is investigated by means of *ab-initio* calculations. The rest of the chapter is organized as follows; Structural properties are given in Section 3.1. Vibrational properties are discussed in Section 3.2. In addition, results of the electronic properties are presented in Section 3.3 and strain-dependent electronic band dispersions are given in Section 3.4. Lastly,our results are summed in Section 3.5.

3.1. Structural Properties

Crystal structure of the single-layer Ge_3N_4, which is shown in Fig.3.1, is formed by a primitive unit cell containing six germanium and eight nitrogen atoms. As viewed from the side perspective, Ge_3N_4 contains two Ge-atomic layers and four N-atomic layers forming a buckled structure. The optimized in-plane lattice parameter of Ge_3N_4 is a=b=8.16 Å. The corresponding Ge-N bond lengths are found to vary between 1.85 and 2.03 Å. Moreover, the thickness of single-layer Ge_3N_4, defined as the distance between the outer-most N atoms, is found to be 2.79 Å. Bader analysis shows that single-layer Ge_3N_4 structure is formed such that each Ge atom donates 1.8 e^- while each N atom recieves 1.3 e^- charge, indicating ionic bond character in the structure. Furthermore, the cohesive energy (E_{Coh}) is found to be 4.08 eV/atom. As compared to well-known 2D materials, such as graphene (10.04 eV/atom) and MoS_2 (9.53 eV/atom), single-layer Ge_3N_4 has a much lower cohesive energy indicating its less energetic stability.[156] On the other hand, the cohesive energy of Ge_3N_4 is lower than that of predicted single-layer nitrides, BN (8.83 eV/atom), AlN (7.15 eV/atom), GaN (6.37 eV/atom), and InN (5.47 eV/atom).[156]

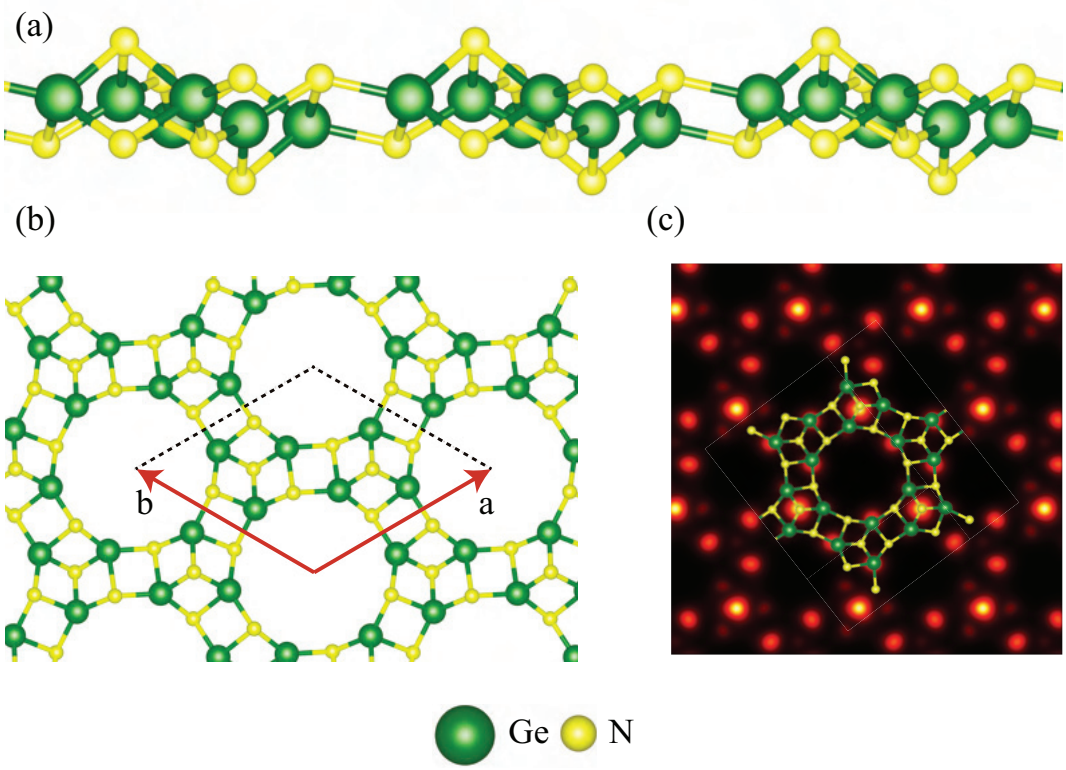

Figure 3.1. For the single-layer of Ge_3N_4; (a) Side and (b) top views of the crystal structure. (c) The simulated STM image.

Mechanical properties of single-layer Ge_3N_4 are calculated in terms of its in-plane stiffness (C) and the Poisson ratio (ν). The calculated in-plane stiffness of single-layer Ge_3N_4 is 62 N/m. As compared to the stifness of well-known single-layers such as MoS_2 (122 N/m)[157] and graphene (340 N/m)[158], single-layer Ge_3N_4 is a soft material. On the other hand, while the stiffness of Ge_3N_4 is lower than that of other nitrides (267, 116, and 110 N/m for BN, AlN, and GaN, respectively), it is comaprable to that of InN (67 N/m).[156] In addition, the Poisson ratio, which is the measure of expansion perpendicular to the direction of compression, is found to be 0.24 and it is between that of MoS_2 (0.26)[157] and graphene (0.19).[158] As compared to planar single-layers of nitrides, Poisson ratio of Ge_3N_4 is higher than that of BN (0.21) while it is much smaller than Poisson ratio of AlN (0.46), GaN (0.48), and InN (0.59) indicating mechanical stability of Ge_3N_4 over other nitride single-layers.[156]

Table 3.1. For the single-layer of G_3N_4; optimized in-plane lattice parameter, a; the vertical distance between the outer-most N atoms, h; the amount of charge donated by a Ge atom and received by a N atom, ρ_{Ge} and ρ_N; the work function, ϕ; calculated cohesive energy per atom, E_{Coh}; electronic band gaps calculated within GGA and HSE06 functionals, E_{Gap} and E_{Gap}^{HSE06}; and the linear-elastic parameters, in-plane stiffnes (C) and Poisson ratio (ν).

	a (Å)	h (Å)	ρ_{Ge} (e^-)	ρ_N (e^-)	ϕ (eV)	E_{Coh} (eV/atom)	E_{Gap} (eV)	E_{Gap}^{HSE06} (eV)	C (N/m)	υ -
Ge_3N_4	8.16	2.79	1.8	1.3	6.38	4.08	1.92	3.27	62	0.24

3.2. Vibrational Properties

In this section, we extend our predictions by confirming the dynamical stability and investigating the lattice dynamics of the free-standing Ge_3N_4 crystal structure through the phonon band spectrum calculations. In order to obtain phonon branches, force constant matrix is generated by the implementation of small displacement method. It is seen that all phonon branches display completely positive phonon eigenvalues through the whole high-symmetry points as presented in Fig.3.2(a), indicating the dynamical stability of free-standing Ge_3N_4 in its ground-state structure. The total 42 phonon branches of single-layer Ge_3N_4 include 13 doubly-degenerate and 13 non-degenerate optical branches. The highest frequency optical phonon branch is found to have a frequency of 869 cm^{-1} at the Γ point, which is much lower than that of BN, in contrast, larger than those for AlN, GaN, and InN indicating quite stronger Ge-N bonds in Ge_3N_4.[156]

The Raman activities of Γ-centered phonon modes are investigated by means of first-order off-resonant Raman calculations, which is suitable for the characterization of the material. As presented in Fig.3.2(a) (right-panel), totally 13 optical branches are found to be Raman active. Among the 13 Raman active modes, we characterize the most prominent 8 phonon modes in terms of their atomic vibrations. The illustrated vibrational motions (see Fig.3.2b) reveal that 4 of the Raman active modes correspond to purely in-plane while 2 of them arise from the out-of-plane vibrations of the atoms. In addition, there are also 2 Raman active modes which consist of coupled in-plane and out-of-plane vibrations. The Raman modes having in-plane vibrational character have frequencies of 223.5, 390.8, 611.0, and 850.7 cm^{-1}. The phonon modes at frequencies 850.7 and 390.8 cm^{-1} are dominated by the vibrations of the inner N atoms, while the peak at 611.0 cm^{-1} mainly

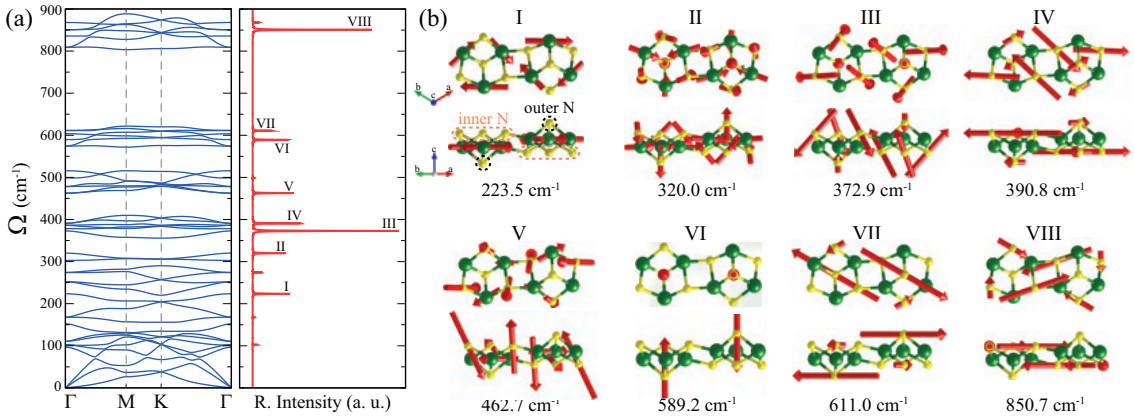

Figure 3.2. For the single-layer of Ge_3N_4; (a) predicted phonon band structure (left panel) and the corresponding Raman activity of zone-centered vibrations (right panel). (b) Illustrated atomic vibrations of various Raman active phonon modes.

arises from vibration of the outer N atoms. Moreover, the lowest frequency in-plane mode (at 235.5 cm^{-1}) stands for the rotational motion of neighboring Ge groups. On the other hand, among the out-of-plane Raman active vibrations, the peak at 589.2 cm^{-1} arises from pure outer N oscillations. In contrast, the phonon mode having frequency of 372.9 cm^{-1} is dominated by the inner N vibrations with slightly weak contribution of outer N atoms. Furthermore, the Raman active modes at 320.0 and 462.7 cm^{-1} correspond to the coupled vibrations of Ge (in-plane) and N (out-of-plane) atoms vibrations. The analysis of the Raman spectrum of single-layer Ge_3N_4 provide deep analysis about the characteristic of its structure.

3.3. Electronic Properties

Electronic properties of single-layer Ge_3N_4 are investigated in terms of the electronic band dispersions. As shown in Fig.3.3, the valence band maximum (VBM) resides between the Γ-M points of the Brillouin Zone while the conduction band minimum (CBM) is located at the Γ point, indicating the indirect band gap nature of single-layer Ge_3N_4. The electronic band dispersions reveal that the top valence states are only dispersive around the Γ point while they are mostly localized through the M-K points. The electronic band gap is calculated to be 3.27 eV. As compared to the predicted electronic band gaps of α-, β-, and

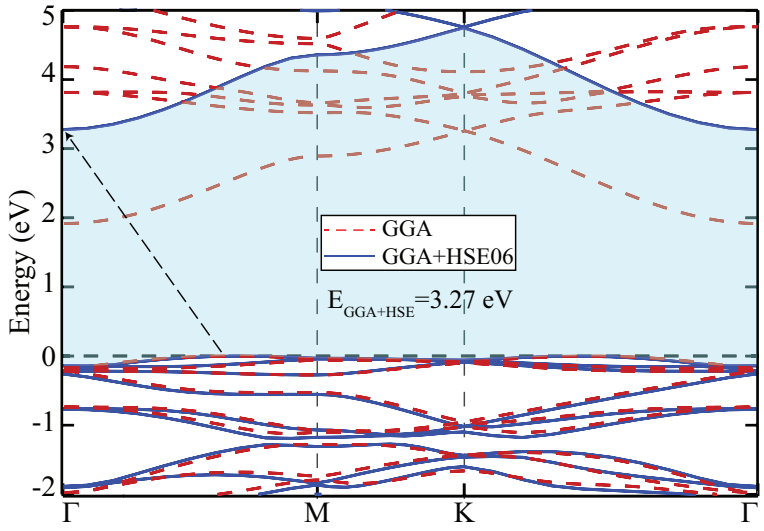

Figure 3.3. Electronic band structure of single-layer Ge_3N_4. Red dashed lines belong to bare GGA band structure while blue lines represent band structure calculated with GGA+HSE06.

γ-Ge_3N_4 phases (3.85 eV, 3.86 eV and 3.56 eV, respectively), single-layer Ge_3N_4 possesses a slightly smaller band gap.[159] In addition, the electronic band gap of single-layer Ge_3N_4 is much smaller than the experimentally observed band gap of γ-Ge_3N_4 (4.50 eV).[160] It is seen that the dimensional reduction from bulk to 2D structure results in the decrease of the electronic band gap. Moreover, the work function of the predicted single-layer Ge_3N_4 is calculated to be 6.38 eV which is much larger than those for single-layers of MoS_2 (5.10 eV) and h-BN (4.70 eV).[?] Apparently, the higher work function of single-layer Ge_3N_4 indicates the localized characteristics of the electron at the top valence state.

Experimental studies have demonstrated that single-layer 2D materials can be used as the building blocks for the formation of van der Waals type heterostructures in order to combine thier electronic properties in a single 2D structure. Fig. 3.4 shows the band alignment of single-layer Ge_3N_4 with several typical 2D single-layers. As shown in Fig. 3.4, the vacuum level of each single-layer is set to zero energy. After the shift of band edge energies by the vacuum energy, the CBM and VBM energies of Ge_3N_4 are found to be -4.33 and -7.49 eV from HSE06, and -4.69 and -6.6 eV from PBE, respectively. In order to make a general conclusion, various single-layer materials from different 2D groups are considered. MoS_2, a famous member of TMDs, GeSe and B-P are choosen as the non-planar single-layers while graphene-like planar structures of h-BN, GaN, and C_2N

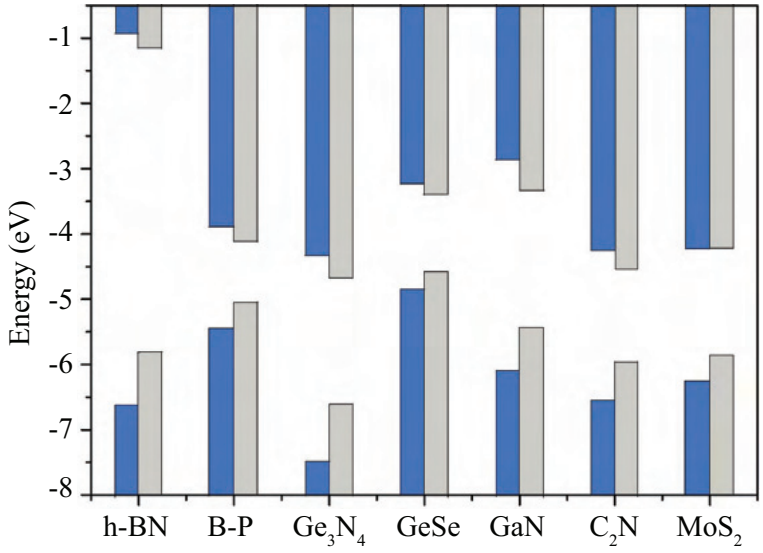

Figure 3.4. Band alignment between Ge_3N_4 and several typical 2D materials. Blue and gray bars indicate results calculated by HSE06 and PBE, respectively. The vacuum energy is set as zero.

are considered as one-atom-thick materials. It is seen that the VBM energy of single-layer Ge_3N_4 is lower than that of other 2D materials considered in our study. Note that while the band gap energy of each single-layer changes with the inclusion of HSE06 in the calculations, the type of the band alignment is not affected by the functional. As shown in Fig. 3.4, single-layer Ge_3N_4 is predicted to form type-II band aligment with all 2D materials except for single-layer GeSe whose VBM and CBM energies are higher than those of Ge_3N_4. This facilitates the separation of electron and holes in van der Waals heterostructures constructed by Ge_3N_4 and these 2D materials, with electron localized on the Ge_3N_4 layer and hole localized on the other layer. In contrast, the GeSe-Ge_3N_4 heterostructure forms a type-I band alignment in which both electron and hole are localized on single-layer Ge_3N_4.

3.4. Strain-dependent properties

Strain is often present in experiments occuring either naturally or controllably and it can alter the electronic properties of materials. Since it is an easy and effective method, strain has often been used to manipulate fundamental properties of ultra-thin ma-

terials.[161,162] In the present section, we present our results on how the electronic structure of single-layer Ge_3N_4 responds against applied uniaxial and biaxial strains. For the investigation of uniaxial strain effect, a rectangular unit cell containing 28-atoms is constructed in order to simulate the strain along the two main orientations in the lattice, namely zigzag (ZZ) and armchair (AC) directions (see Fig.3.5(a)).

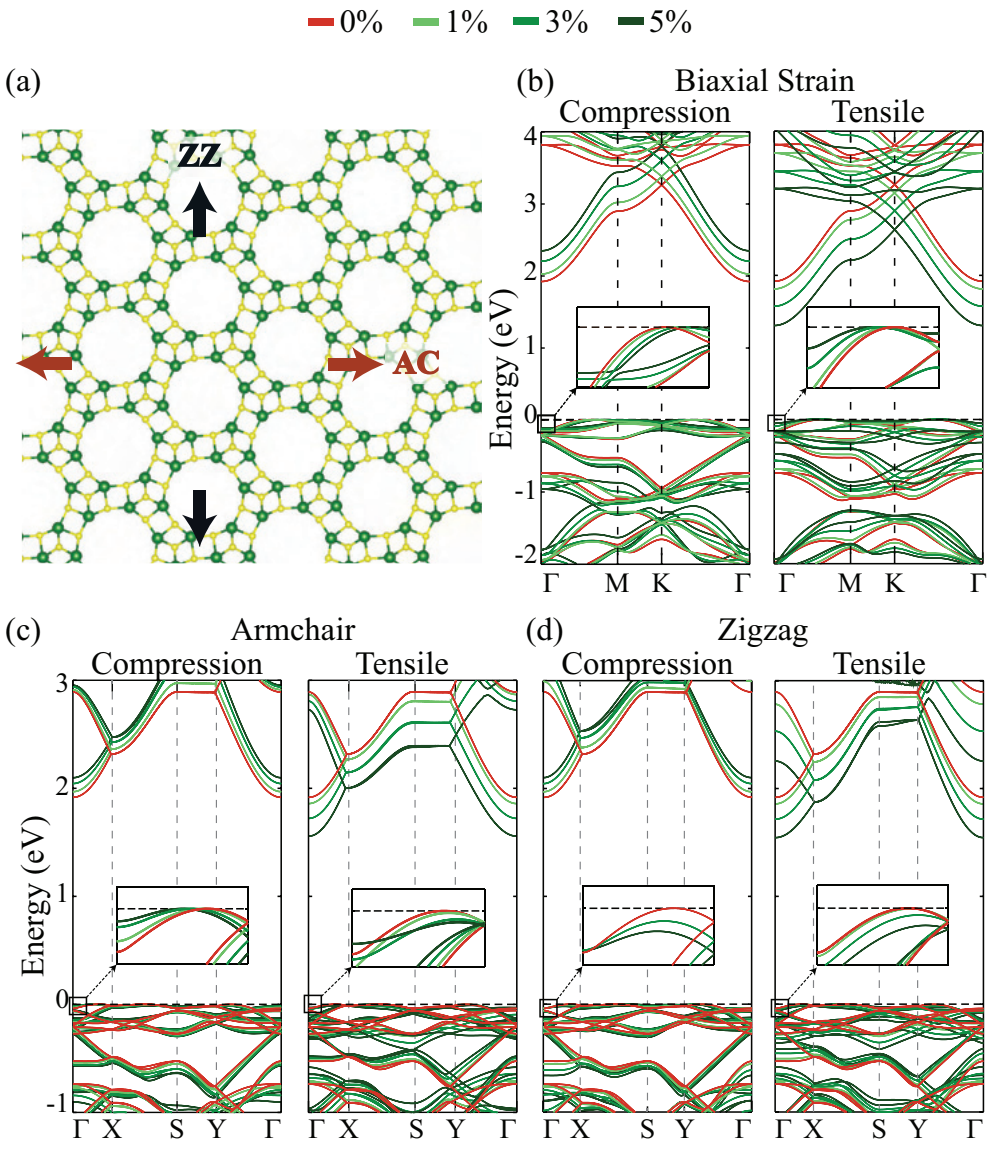

Figure 3.5. (a) AC and ZZ orientations of single-layer Ge_3N_4 with rectangular unit cell. The electronic band diagrams of single-layer Ge_3N_4 under (b) biaxial strain, (c) uniaxial strain on AC orientation, (d) uniaxial strain on ZZ orientation.

Effects of uniaxial as well as biaxial strains on the electronic band dispersions are calculated by changing the lattice parameters by $\pm$ 1 %, $\pm$ 3 % and $\pm$ 5 % amounts both in

tensile and compressive cases. The results for the biaxial strain are presented in Fig. 3.5(b). It is seen that the CBM of single-layer Ge_3N_4 displays shift to lower energies via applied tensile biaxial strain while it shifts to higher energies under compressive strain. As a result of those shifts of the CBM, the electronic band gap is found to change from 1.30 eV (at 5% of tensile biaxial strain) to 2.34 eV (at 5% of compressive biaxial strain). Note that the indirect gap behavior of Ge_3N_4 is robust against the applied biaxial strain regardless of the strain type, compressive or tensile. In addition, while the location of VBM does not change via biaxial strain, the energy of the valence states at the Γ point increases under tensile strain resulting in less dispersive states residing between the Γ-M points.

On the other hand, our results for the applied uniaxial strains are shown in Figs. 3.5(c) and (d) (for AC and ZZ directions, respectively). Note that since a rectangular cell is used for the uniaxial strain, the high symmetry points are given in the corresponding frame. It is seen that regardless of the strain direction, the energy of the CBM displays a shift to higher (lower) energies via applied compressive (tensile) strain. However, in all cases the CBM resides at the same point under applied uniaxial strain. As zoomed out in the insets of Figs. 3.5(c) and (d), the compressive uniaxial strain along AC direction exhibits a similar effect with that of tensile biaxial strain for the valence state residing between the Γ-M points. It is found that the electronic band gap decreases (increases) via uniaxial tensile (compressive) strains. The energy band gap ranges from 1.56 eV (at 5% of tensile uniaxial strain) to 2.10 eV (at 5% of compressive uniaxial strain) in both directions. It is clear that the indirect nature of the electronic band gap is not affected by the type or direction of the uniaxial strain while the band gap changes depending on the strength of the strain. The mechanism behind such change can be found in the atomic orbital contributions to the lowest conduction and highest valence states. It is found that the CBM state is formed by the in-plane orbitals of the atoms, which indicates that those states are more sensitive to the applied in-plane strain. In contrast, the VBM state is dominated by the out-of-plane orbitals of the individual atoms and thus, VBM is mostly unaffected by the in-plane strain.

3.5. Conclusions

In summary, I performed DFT-based first-principles calculations in order to investigate the structural, vibrational and electronic properties of single-layer Ge_3N_4 and the

effects of biaxial and uniaxial strains on the electronic properties were reported. Geometry optimization revealed that single-layer Ge_3N_4 possesses a holey buckled structure. Phonon band dispersion calculations showed that single-layer Ge_3N_4 is dynamically stable. Further investigations on vibrational properties indicated that Raman active phonon modes can be used as key for the identification of single-layer Ge_3N_4 via Raman spectroscopy. Moreover, the electronic properties of single-layer Ge_3N_4 were investigated in terms of the electronic bands and it was shown that Ge_3N_4 is a large gap semiconductor with an indirect band gap behavior. In addition, it was also predicted that single-layer Ge_3N_4 forms type-II vdW heterostructures with various one-atom-thick and puckered 2D materials except for single-layer GeSe which gives rise to a type-I band alignment. Furthermore, it was found that independent of the type of the applied strain, biaxial or uniaxial, single-layer Ge_3N_4 preserves its indirect gap nature while its electronic band gap is tunable with external strain. Single-layer Ge_3N_4 can be considered as a potential candidate for nanoelectronic applications with its strain-tunable band gap.

CHAPTER 4

BAND GAP ENGINEERING OF VAN DER WAALS HETEROSTRUCTURES OF AlAs AND InSe: EFFECT OF EXTERNAL ELECTRIC FIELD

Group III-V semiconductors have been well-known owing to their electronic and optical properties such as exceptional light emission, high electron mobility, good miscibility, high melting point and direct band-gap.[94,95,96] Such properties make them to be potential candidates in applications of lasers,[97,98,99] solar cells,[100,101] light emitting diodes,[102,103] nanowires,[104,105,106] and valleytronics.[107] Bulk aluminum arsenide (AlAs), a member of group III-V semiconductors family, exhibits high electron mobility and a narrow band gap.[94] At ambient conditions, bulk AlAs exists in a stable zinc-blende structure[95] while different phases and transitions between the phases were reported to be feasible.[108,109,110] It was shown that reduction of resistance in bulk AlAs and the variation of electron transport properties were observed under compressive pressure.[111] On the other hand, naturally occurring defects in zinc-blende form of AlAs were reported to be similar to those of in GaAs, and Mg doping was shown to result in p-type conductivity.[112] In addition, for the quantum wells of AlAs it was demonstrated that doping has improved electron mobility[113] while atomic substitution of Al with V and/or Ti caused ferromagnetisim.[114] In another study, oxidation of AlAs films were investigated under ultra-high vacuum conditions, and it was found that water can oxidize AlAs more effectively than O_2.[115] Moser et al. produced heavy-mass, multivalley quantum wires consisting of AlAs.[116] Apart from those reports, AlAs has also been widely used in heterostructures and alloys especially with GaAs due to their well-matching lattice constants.[117,118,119,120,121,122,123,124,125]

As a recent member of 2D materials, single layer form of InSe exhibiting high electron mobility at room temperature has been widely considered as a suitable building block of heterostructures.[126,127] It was reported that in ultraviolet and infrared region, single layer InSe exhibits considerable photo-transistor characteristics making it a potential candidate for photo-detector applications.[128,129] Moreover, reports revealed that InSe is durable under strain[130] and possesses strain-dependent electronic features,[131] which favors

its use in electromechanical applications and in gas sensors.[132]

In the present work, motivated by the recent synthesis of single layer AlSb,[133] an analogue of AlAs single layer, vertical heterostructures of AlAs and InSe were predicted. Structural, electronic and vibrational properties of four possible stacking configurations of the formed heterostructure were investigated. It was shown that as In atom of InSe lies on top of As atom the optimized structure corresponds to the most energetic stacking sequence. Structural optimizations revealed that two H- and two T-phases of the heterostructure can be formed and the two phases are distinguished, by means of their Raman spectra. Electronically, it was shown that two indirect band gap semiconductors of InSe and AlAs form a direct band gap semiconductor as the layers interact via van der Waals forces. Moreover, effect of an external electric field perpendicular to the layer plane was applied in a range of ± 0.5 V/Å and the results indicated the tuning of electronic features by means of energy band gap and band alignment of the heterojunction.

4.1. Single Layers InSe and AlAs

Optimized lattice parameters for single layer InSe and AlAs are 4.04 Å and 4.00 Å respectively. As listed in Table. 4.1, the In-Se and Al-As bond lengths are 2.67 and 2.46 Å, respectively. From the results of the Bader charge analysis, it is seen that In atoms donate 0.6 e to Se atoms when forming InSe while for AlAs there is 1.9 e transfer from Al atoms to As atoms. Calculated work functions of single layer structures are 5.80 eV for InSe and 5.12 eV for AlAs.

Electronic band dispersions (Fig. 4.1b.) indicate that both InSe and AlAs are indirect band gap semiconductors. It was experimentally shown that single layer InSe is an indirect semiconductor with a band gap of 2.90 eV.[134] The calculated band gap of InSe is slightly lower (2.41 eV) than that of the experimental observation.

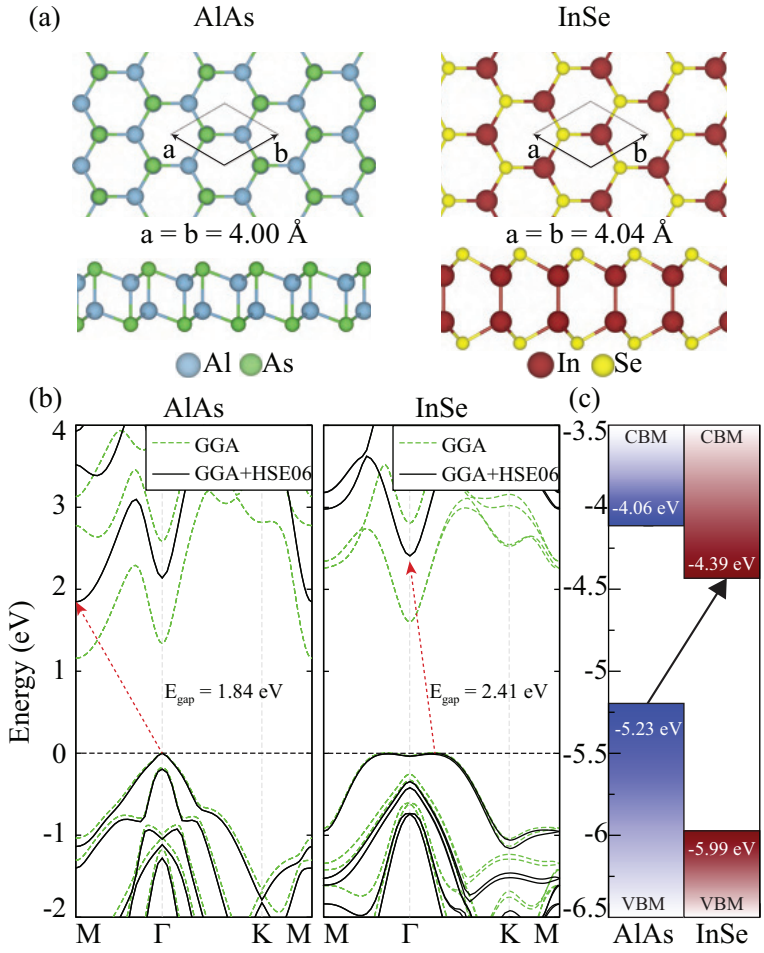

Figure 4.1. For the optimized single layers AlAs and InSe, (a) top and side views of each structure, (b) electronic band dispersions, and (c) band alignment of their heterojunction.

Calculated electronic band dispersions of InSe reveal that its valence band maximum (VMB) resides at the M-Γ point while conduction band minimum (CBM) is located at the Γ point of the BZ. On the other hand, calculated VBM of AlAs is located at the Γ point while its CBM resides at the M point indicating the semiconducting nature of AlAs with a band gap of 1.84 eV.

As shown in Fig. 4.2, free-standing single layers of AlAs and InSe are dynamically stable 2D crystals. Phonon band dispersions of the both single-layer structures are free from any imaginary frequencies through the whole BZ. It is found that each single-layer structure exhibits nine optical phonon branches, out of the three acoustical phonons. In the case of single-layer AlAs, there are three doubly-degenerate phonon modes while

Table 4.1. Calculated ground state properties of single layers AlAs and InSe; the optimized in-plane lattice parameters, a=b, the vertical distance between the outer-most atoms, h, the atomic bond lengths between different atoms within the structures, d_{X-Y}, the work function, ϕ, and electronic energy band gap within approximations GGA, E_g^{GGA}, and GGA+HSE06, E_g^{HSE06}.

	a (Å)	h (Å)	d_{In-Se} (Å)	d_{Al-As} (Å)	ϕ (eV)	E_g^{GGA} (eV)	E_g^{HSE06} (eV)
AlAs	4.00	3.44	-	2.46	5.12	1.16	1.84
InSe	4.04	5.44	2.67	-	5.80	1.60	2.41

the remaining three modes are non-degenerate at the zone-center (Γ point). Similarly, single-layer InSe possesses three doubly-degenerate and three non-degenerate phonon branches as a result of the hexagonal symmetry of the structure. On the right panel of the Fig. 4.2 (c and d), the vibrational motion of the individual atoms in each phonon modes are given by red and blue arrows. The three non-degenerate modes of AlAs are found to be at frequencies 168, 258, and 329 cm^{-1} while the doubly-degenerate modes have frequencies 93, 340, 362 cm^{-1}.

The mode at 93 cm^{-1} arises from the shear-like vibration of top and bottom Al-As pairs in the in-plane direction, while the mode having frequency 168 cm^{-1} stems from the out-of-phase vibration of As atoms along the out-of-plane direction. In addition, the phonon mode at frequency 258 cm^{-1} is dominated by the vibration of Al atoms and represents the opposite vibration of Al-As atoms residing at the same atomic plane. On the other hand, the phonon mode having frequencies 329 cm^{-1} arises from the in-plane opposite vibration of top and bottom Al-As pairs. Similarly, phonon mode at 362 cm^{-1} shows the out-of-phase vibration of same type of atoms and it is dominated by the Al vibrations. The phonon branch at 340 cm^{-1}, however, stems from the out-of-plane vibration of Al and As atoms, where Al atoms vibrate in-phase while Al and As atoms vibrate oppositely.

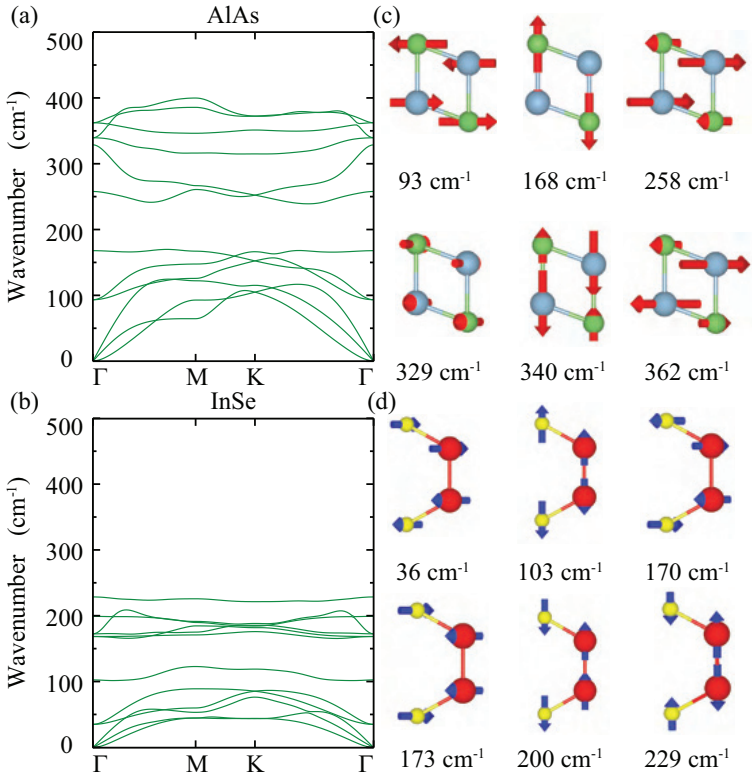

Figure 4.2. Phonon band dispersions of single layer (a) AlAs and (b) InSe. For AlAs (c) and InSe (d), the vibrational motion of individual atoms in optical phonon modes represented at the Γ point of the BZ.

In the case of InSe, the phonon modes at frequencies 36 and 103 cm^{-1} represent the shear-like and breathing-like vibrations of top and bottom In-Se pairs with respect to each other, respectively. In the mode at frequency 170 cm^{-1}, both In and Se atoms vibrate out-of-phase while the phonon mode having frequency 173 cm^{-1} arises from the opposite vibration of In and Se pairs in the in-plane direction. On the other hand, the remaining two phonon modes at frequencies 200 and 229 cm^{-1} represent the out-of-plane vibration of In and Se pairs and top-bottom In-Se pairs, respectively.

4.2. van der Waals Heterostructures of AlAs and InSe

For the formation of heterostructure of AlAs and InSe layers, four different stacking orders (the most symmetric stackings) are constructed. As shown in Fig. 4.3(a), the four stacking orders refer to the alignments of the atoms such that In atoms reside on top

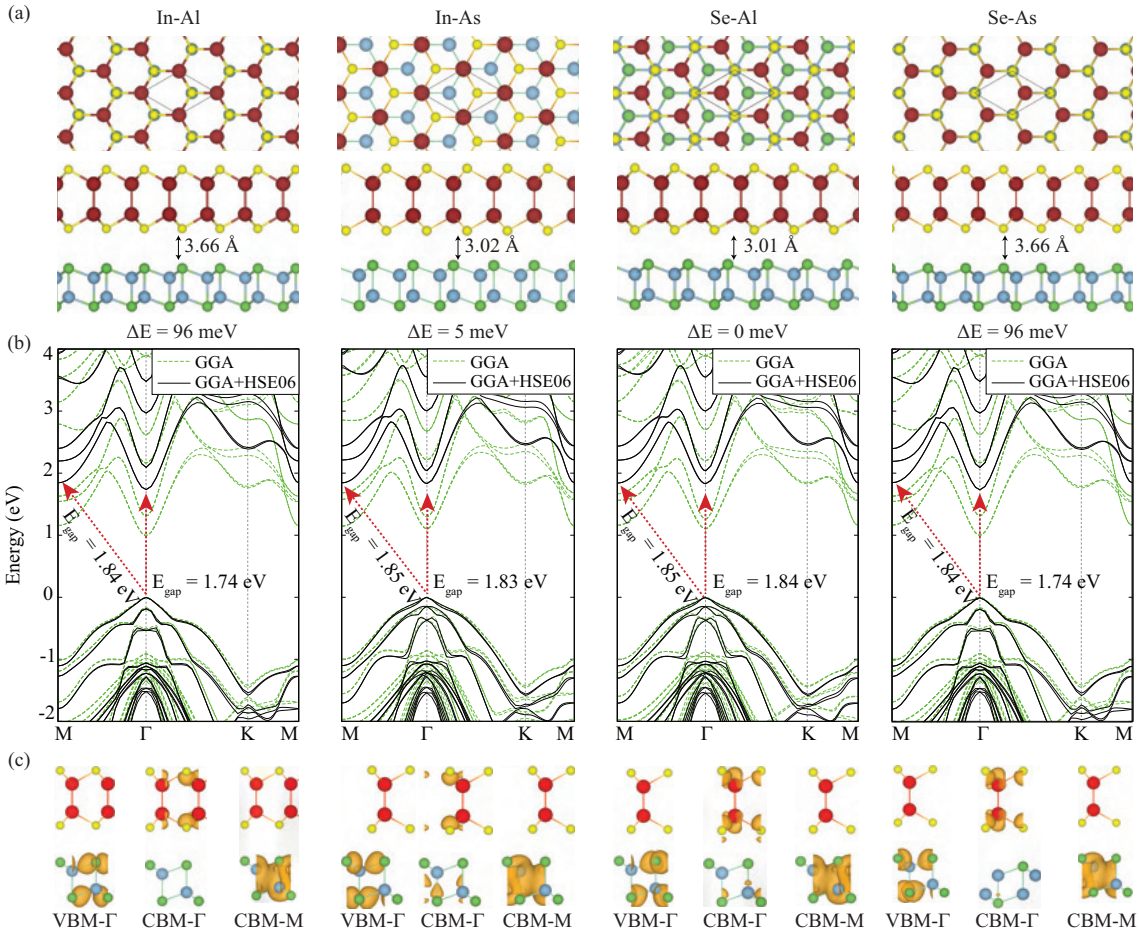

Figure 4.3. For the different stacking orders of the heterostructure, (a) top view and side view of the structures, (b) electronic band dispersions and (c) charge densities of VBM at the Γ point, and CBM at the Γ point and the M points.

of Al atoms (namely 2H-phase) and In atoms are located on top of As (1T-phase of heterostructure). The other two stackings are formed with respect to the alignment of Se atoms on AlAs layer. Similarly, the 2H-phase is formed such that Se atoms reside on top of As atoms, the alignment of Se atoms on Al atoms gives rise to the 1T-phase formation.

The optimized lattice parameters of single layers AlAs (4.00 Å) and InSe (4.04 Å) are close to each other, the induced strains on the layers in the heterostructures are ±0.5%. For layer-layer interaction energies, namely the binding energies, the ground state stacking configuration is found to be the one in which Se atoms reside on Al atoms. Notably, the second most energetic stacking (In atoms are aligned on As atoms) has a binding energy which is only 5 meV lower than that of the ground state stacking. The

binding energies are calculated to be 285 and 280 meV for the two most energetic stackings, respectively. In both stacking configurations, the heterobilayer structure crystallizes in 1T-phase. On the other hand, the other two stackings referring to the 2H-phase exhibit relatively lower binding energies (each 188 meV). While the optimized in-plane lattice parameters of each stacking sequence is the same (4.02 Å), the interlayer distance show dissimilarity between 2H- and 1T-phases. For the two most energetic stackings, the layer-layer distances are 3.01 and 3.02 Å, respectively, while for the 2H-phase stackings the distance is 3.66 Å. Apparently, the alignment of either In or Se atoms on the hollow site of AlAs layer increases the layer-layer interaction and results in smaller interlayer distance. In all stacking formations, the bond lengths between the individual atoms of each layer remain the same since the induced strains are small.

Vibrational properties of materials in terms of their Raman spectra are useful since it is possible that different structural phases of a material or stacking orders in heterostructures can be identified through Raman measurements. By using the Raman spectrum of a heterostructure, it is possible to distinguish between different stacking orders considering the frequency shifts of the phonon modes and the change in the corresponding Raman activities. As the layer-layer vdW interaction exist, the low-frequency Raman modes originating from the weak vdW interaction become experimentally observable.

The Fig. 4.4 shows the full Raman spectrum of each stacking sequence for the InSe/AlAs heterobilayers. The frequency regime between 0-50 cm^{-1} is zoomed out since the calculated Raman activities of the phonon modes in the range are much smaller than those of the high-frequency modes. For vdW-type layered and heterostructure materials, the low-frequency regime includes the interlayer vibrations and in the case of InSe/AlAs heterobilayers one of the individual phonon mode of InSe layer falls also into this regime. The interlayer shear mode (SM) and the layer-breathing mode (LBM) represent the rigid vibration of AlAs and InSe layers with respect to each other along the in-plane and out-of-plane directions, respectively. Apart from the phonon frequencies, the Raman activities of the three low-frequency modes can be used to identify the stacking type and the lattice symmetry. Apparently, the 1T and 2H-phase heterobilayers are distinguishable in terms of the Raman activities of the low-frequency phonon modes. In addition, the frequencies of SM/LBM modes are calculated to be 10/26, 15/29, 16/30, and 10/26 cm^{-1} for the stacking sequences of In-Al, In-As, Se-Al, and Se-As, respectively. It is apparent that

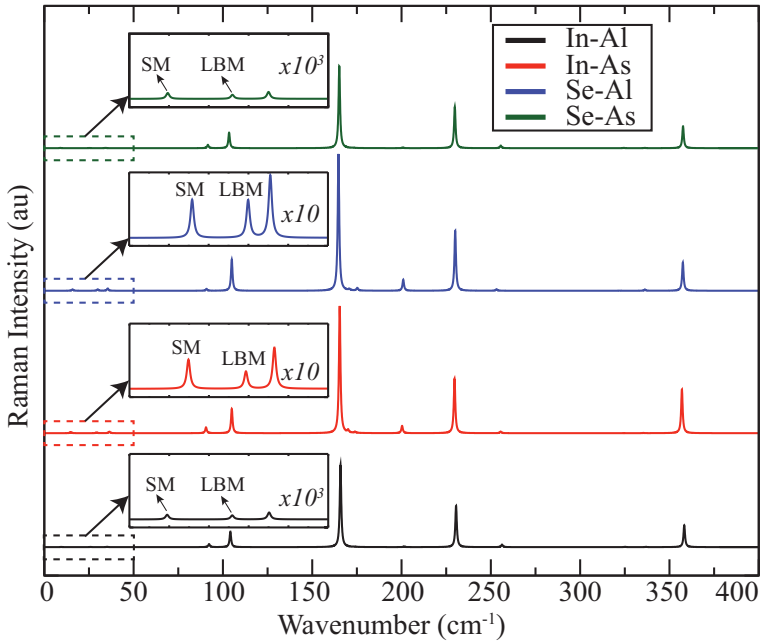

Figure 4.4. Raman spectrum of each stacking order in the heterobilayer. The low-frequency regime of each spectra are highlighted for comparison.

the two lowest energy stackings (corresponding to 1T-phase) are distinguishable from the 2H-phase stacking orders. Moreover, the phonon mode stemming from the vibration of In-Se atoms in InSe layer is found to have the same frequency in three stacking orders (35 cm^{-1}) except for the Se-Al stacking (36 cm^{-1}). While its Raman activity can be used to distinguish between the two phases of heterobilayers, its frequency does not allow one to identify different stacking orders except for the Se-Al stacking. Notably, the frequency of the mode is almost independent of the layer-layer interactions since it arises from an individual layer only.

Similar to the low-frequency regime, high-frequency phonon modes are also important for the identification of structural phases and layer-layer orientations. As presented in the Fig. 4.4, the most intense Raman peak appears to be at the frequency 170 cm^{-1} for the In-Al, In-As, and Se-As stackings and 171 cm^{-1} for the Se-Al stacking order. Sice it arises from the atomic vibrations of InSe layer, its frequency is not significantly affected by the stacking order. The Raman activity of the phonon mode is higher for the 1T-phase stacking orders (In-As and Se-Al). In addition, the phonon mode of InSe at frequency 174-175 cm^{-1} appears as a shoulder near the mode at 170 cm^{-1} in 1T-phase structures while its

Table 4.2. For the four different stacking orders of InSe/AlAs heterosbilayer; layer-layer interaction energy, E_{int}, interlayer distance, d_{L-L}, the work functions calculated from two surfaces, ϕ_{Se} and ϕ_{As}, band gap energies calculated within GGA, E_g^{GGA}, and GGA+HSE06, E_g^{HSE06}, and the type of the band alignment.

	E_{int}	d_{L-L}	ϕ_{Se}	ϕ_{As}	E_{Gap}^{GGA}	E_{Gap}^{HSE06}	Band
	(meV)	(Å)	(eV)	(eV)	(eV)	(eV)	Alignment
In-Al	188	3.66	5.15	5.10	0.99	1.74	Type-II
In-As	280	3.02	5.27	5.15	1.11	1.83	Type-II
Se-Al	285	3.01	5.23	5.15	1.12	1.84	Type-II
Se-As	188	3.66	5.19	5.14	0.99	1.74	Type-II

activity is not observable in 2H-phase stackings. On the other hand, in the frequency regime between 200-250 cm^{-1}, there exist two prominent Raman active phonon modes, which arise from the InSe layer, for the In-As and Se-Al stackings. In contrast, for the 2H-phase stackings a single prominent peak is calculated at 230 cm^{-1}. It can be pointed out that the 1T- and 2H-phases can also be distinguished through the two modes of InSe layer in terms of the Raman activities. Although, an additional prominent Raman peak is found to exist at 358 cm^{-1}, neither its frequency nor its Raman activity can be used to identfy the structural phase and the stacking order.

Electronic properties of the AlAs/InSe heterobilayers are investigated through the electronic band dispersions of each stacking (see Fig.4.3(b)). As shown in Fig. 4.1(c), the proposed band alignment of the isolated AlAs and InSe layers is a type-II heterojunction in which the top valence and bottom conduction states originate from AlAs and InSe layers, respectively. Such type of band alignment allows the formation of interlayer excitons whose electrons and holes originate from different layers. Although, each isolated layer is indirect band gap semiconductor, the type-II heterojunctions possess direct energy band gap whose VBM and CBM states reside at the Γ point. The calculated energy band gaps (see Table II) reveal that the layer-layer interaction energy results in increase of the energy band gap as it gets stronger. In the case of ground state stacking order, the electronic band gap energy is calculated to be 1.84 eV. Notably, in the 2H-phase stackings, the energy

difference between conduction states at the M and the Γ points is larger as compared to that in 1T-phase structures. As shown in the Fig. 4.3(b), the direct and indirect band gap energies are very close to each other in In-As and Se-Al heterobilayers exhibiting 1T-phase structure. The energy difference between the indirect and direct band gaps are around 10 to 20 meV which make the direct-indirect transitions quite possible. In addition, for the two electronic behaviors there exist two different heterojunction types. As presented in the Fig. 4.3(c), while the VBM at the Γ point is fully dominated by the AlAs states, the conduction band edges at the M and the Γ points arise from two different layers. The indirect band gap between the Γ-M points gives rise to the formation of type-I heterojunction while the direct band gap behavior at the Γ point results in the type-II heterojunction formation. Such close energies reveal that the direct-indirect transitions or type-I/type-II transitions, in the electronic band gap behavior can be achieved by external effects such as electric field or strain.

4.3. Effect of External Electric Field

Nanodevices are usually subjected to external electric field or namely gating in order to tune the performance of the device. In case of a heterostructure, when it is applied in an optoelectronic nanodevice, the heterostructure can be controllably subjected to an external electric field which may cause a change in its electronic properties. In order to investigate such tunable properties, AlAs-InSe heterobilayer structure is subjected to an electric field pointing along the out-of-plane direction. For the applied field, both $\pm z$ directions are considered such that the field operates either from InSe to AlAs (negative field) or from AlAs to InSe (positive field). The strength of the applied field varies from 0.1 to 0.5 V/Å for both directions. Note that, for the application of the electric field, only the ground state stacking configuration is taken into account.

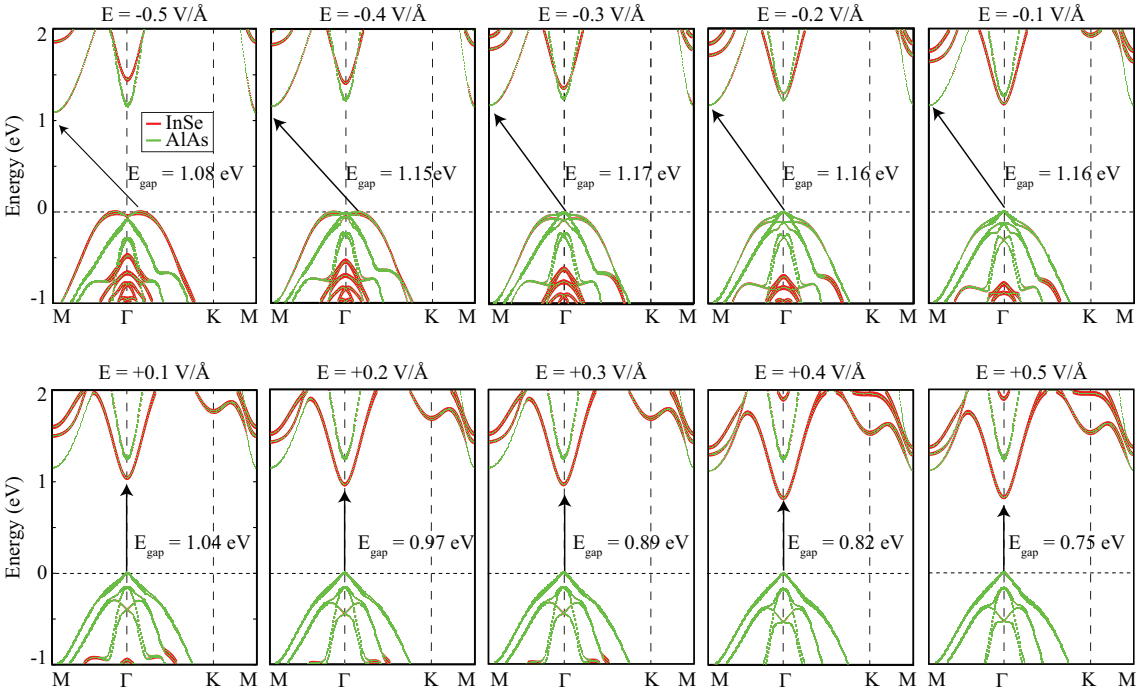

Figure 4.5. The layer-decomposed electronic band structures of the heterostructure under external electric field. The red and green curves stand for the states of InSe and AlAs, respectively.

The Fig. 4.5 shows evolution of the layer-decomposed electronic band dispersions under applied electic field. As the external electric field, ε_{ext}, points from AlAs layer to InSe, the direct band gap nature of the heterobilayer is found to be conserved under increasing field strength. Apparently, the conduction band edge at the M point (originating from AlAs layer) shifts upward while that of residing at the Γ point (stemming from InSe layer) shifts to lower energies indicating that the energy difference between the CBM states of the individual layers increases. On the other hand, the VBM state of the heterostructure remains to reside at the Γ point with increasing field strength and the type-II band alignment is preserved. As shown in the Fig. 4.5, the band gap energy varies linearly with the strength of ε_{ext} as the field points towards InSe layer. Such linear behavior can be explained through the interaction mechanism between the band edges of the individual layers. Under positive ε_{ext}, while the energies of conduction band edges of AlAs (InSe) shift upward (downward), the electrons are still confined to each layer, separately. In contrast, the energy level of VBM states arising purely from InSe layer display downward shift while that of stemming from AlAs almost remains the same. Notably, within range of

applied positive ε_{ext} the layers do not exhibit hybridization and therefore, the band offset energies tuned by the external field is linear, leading to linear decrease of the energy band gap. The confinement of electrons in the out-of-plane direction in each layer does not lead to hybridization between the constituent layers and thus, the band gap variation is linear (see the blue region of the Fig.4.6).

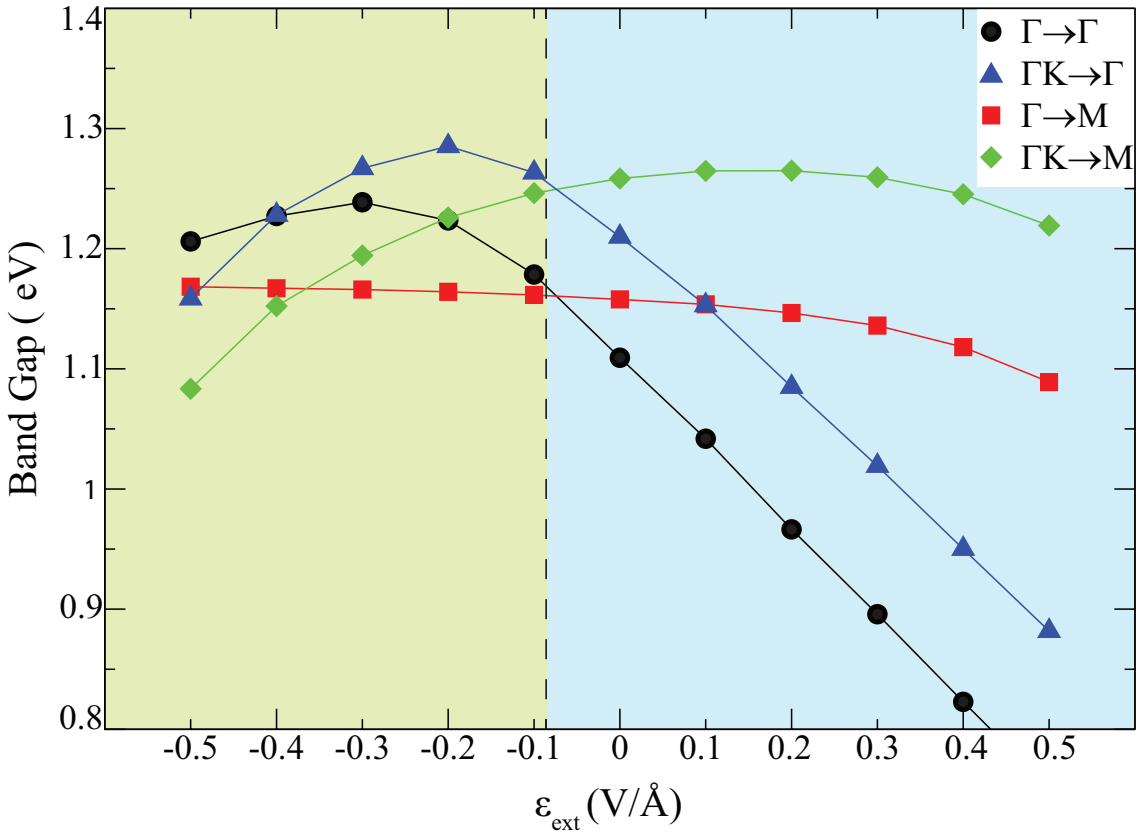

Figure 4.6. The layer-decomposed electronic band structures of the heterostructure under external electric field. The red and green curves stand for the states of InSe and AlAs, respectively.

For the negative external field, a different physical mechanism dominates the behavior of the electronic bands and the corresponding energy band gap. When the applied ε_{ext} points from InSe towards the AlAs layer, the conduction band edges of AlAs layer lying at the M and the Γ points shift downward while those of InSe shift oppositely. Since the CBM of the heterostructure shifts to the M point, there occurs direct to indirect band gap transition at -0.08 V/Å of the applied field. As the field strength increases, the VBM state at the Γ point originating from AlAs layer shifts to lower energies. For the field

strengths of -0.1, -0.2, and -0.3 V/Å, the VBM of the heterostructure stems from AlAs layer and resides at the Γ point. A transition from type-II to type-I heterojunstion is seen within the -0.3$>\ \varepsilon_{ext}\ >$-0.08 V/Å of the applied field. As seen from the Fig. 4.5, for negative ε_{ext} the valence states of two layers around the Γ point (through the paths M-Γ and Γ-K) start to overlap and the hybridized bands appear. Therefore, the holes are not anymore confined to each layer and are distributed across both layers around the Γ point. As the ε_{ext} is -0.08 V/Å, the electronic band gap transition is favorable between Γ-M while over -0.3 V/Å Γ/K-M transitions become feasible. Thus, the change of the band gap is represented by the black dots between 0.5 and -0.08 V/Å and then followed by the red squares up to -0.4 V/Å of the applied field. Finally, for ε_{ext} values over -0.4 V/Å, the change in the band gap is shown by the green diamonds. Apparently, both energy shifts of the band edges of constituent layers and the hybridization of valence states of the layers drive the behavior of the energy band gap in the yellow region shown in Fig. 4.6).

4.4. Conclusions

A van der Waals type heterobilayer structure formed by InSe and AlAs layers was predicted by means of first-principles calculations. For the dynamically stable single layers of InSe and AlAs, it was shown that four different stacking configurations can be formed. Raman spectrum analysis revaled that the most energetic two stacking order configurations are distinguishable in terms of the low-frequency interlayer phonon modes. In addition, electronically it was shown that in all four stacking orders the two indirect band gap semiconductors (InSe and AlAs isolated layers) form direct band gap semiconductor in type-II staggered-gap band alignment in which AlAs dominates the highest energy holes as well as the lowest energy electrons are separated in InSe layer. Moreover, the effect of an external out-of-plane electric field on the electronic properties was investigated by means of the energy band dispersions and the band gap energy. The results showed that due to the out-of-plane asymmetry in the formed heterobilayer, not only the strength but also the direction of the field affects the electronic behavior of the heterobilayer. The heterostructure was found to display a transition from direct to indirect band gap under negative electric fields while it was shown to be robust direct band gap semiconductor for positive fields. It was further revealed that for the electric fields with strengths up to -0.3

V/Å, the heterobilayer structure possesses a transition from type-II to type-I heterojunction while for stronger fields along the same direction overlapping of valence states of each layer occurs. Consequently, the van der Waals type heterobilayer of InSe and AlAs with well-controlled electronic features under external field is predicted to be suitable for applications in optics and optoelectronics.

CHAPTER 5

OVERALL DISCUSSION

Overall, motivated by the outstanding physics of electrons in low-dimensions, this master thesis focused on the investigation and the characterization of different types of novel ultra-thin crystals by means of DFT-based first-principles calculations.

In 1st chapter, a short introduction is written related to the 2D materials while 2nd chapter is the methodology of the DFT.

In the work given in Chapter 3, a novel 2D material, Ge_3N_4 is proposed which is both structurally and dynamically stable. Electronic band dispersions show that single-layer Ge_3N_4 is a indirect band gap semiconductor whose band gap is tunable with applied strain, while indirect nature is not affected.

Chapter 4 is the investigation of the effect of external electric field on the properties of AlAs/InSe heterobilayer. A stable indirect semiconductor single layer structure of AlAs is proposed. The resulted heterobilayer from the combination of AlAs/InSe is a direct band gap semiconductor. When a negative external electric field is applied to heterostructure, Type II - Type I transition occurs along with direct - indirect gap transition.

To conclude, this thesis propose novel graphene like single layer structures and their heterostructure based on the first-principles calculations. Structural, electronic and vibrational investigations reveal that Ge_3N_4, AlAs, Inse and AlAs/InSe heterostructure can be used in various nanotechnology applications.

REFERENCES

(1) Novoselov, K. S.; Geim, A. K.; Morozov, V. S.; Jiang, D.; Zhang, Y.; Dubonos, V. S.; Grigorieva, V. I.; Firsov, A. A. Electric field in atomically thin carbon films. *Science* **2004**, *306*, 666–669.

(2) Neto, A. H. C.; Guinea, F.; Peres, N. M. R.; Novoselov, K. S.; Geim, A. K. The electronic properties of graphene. *Reviews of Modern Physics* **2009**, *81*, 109.

(3) Geim, A. K. Graphene: Status and Prospects. *Science* **2009**, *324*, 1530–1534.

(4) Lu, J. P. Elastic properties of carbon nanotubes and nanoropes. *Physical review letters* **1997**, *79*, 1297.

(5) Mayorov, A. S.; Gorbachev, R. V.; Morozov, S. V.; Britnell, L.; Jalil, R.; Ponomarenko, L. A.; Blake, P.; Novoselov, K. S.; Watanabe, K.; Taniguchi, T. Micrometer-scale ballistic transport in encapsulated graphene at room temperature. *Nano letters* **2011**, *11*, 2396–2399.

(6) Morozov, S.; Novoselov, K.; Katsnelson, M.; Schedin, F.; Elias, D.; Jaszczak, J. A.; Geim, A. Giant intrinsic carrier mobilities in graphene and its bilayer. *Physical review letters* **2008**, *100*, 016602.

(7) Balandin, A. A. Thermal properties of graphene and nanostructured carbon materials. *Nature materials* **2011**, *10*, 569–581.

(8) Lee, C.; Wei, X.; Kysar, J. W.; Hone, J. Measurement of the elastic properties and intrinsic strength of monolayer graphene. *science* **2008**, *321*, 385–388.

(9) Nair, R. R.; Blake, P.; Grigorenko, A. N.; Novoselov, K. S.; Booth, T. J.; Stauber, T.; Peres, N. M.; Geim, A. K. Fine structure constant defines visual transparency of graphene. *Science* **2008**, *320*, 1308–1308.

(10) Bunch, J. S.; Verbridge, S. S.; Alden, J. S.; Van Der Zande, A. M.; Parpia, J. M.; Craighead, H. G.; McEuen, P. L. Impermeable atomic membranes from graphene sheets. *Nano letters* **2008**, *8*, 2458–2462.

(11) Moser, J.; Barreiro, A.; Bachtold, A. Current-induced cleaning of graphene. *Applied Physics Letters* **2007**, *91*, 163513.

(12) Elias, D. C.; Nair, R. R.; Mohiuddin, T.; Morozov, S.; Blake, P.; Halsall, M.; Ferrari, A. C.; Boukhvalov, D.; Katsnelson, M.; Geim, A. Control of graphene's properties by reversible hydrogenation: evidence for graphane. *Science* **2009**, *323*, 610–613.

(13) Loh, K. P.; Bao, Q.; Ang, P. K.; Yang, J. The chemistry of graphene. *Journal of Materials Chemistry* **2010**, *20*, 2277–2289.

(14) others,, et al. Fluorographene: a two-dimensional counterpart of Teflon. *small* **2010**, *6*, 2877–2884.

(15) Nair, R. R.; Wu, H. A.; Jayaram, P. N.; Grigorieva, I. V.; Geim, A. K. Unimpeded Permeation of Water Through Helium-Leak–Tight Graphene-Based Membranes. *Science* **2012**, *335*, 442–444.

(16) Shetti, N. P.; Malode, S. J.; Nayak, D. S.; Bagihalli, G. B.; Reddy, K. R.; Ravindranadh, K.; Reddy, C. V. A novel biosensor based on graphene oxide-nanoclay hybrid electrode for the detection of Theophylline for healthcare applications. *Microchemical Journal* **2019**, *149*, 103985.

(17) Kumar, S.; Bukkitgar, S. D.; Singh, S.; Singh, V.; Reddy, K. R.; Shetti, N. P.; Venkata Reddy, C.; Sadhu, V.; Naveen, S. Electrochemical sensors and biosensors based on graphene functionalized with metal oxide nanostructures for healthcare applications. *ChemistrySelect* **2019**, *4*, 5322–5337.

(18) Cakici, M.; Kakarla, R. R.; Alonso-Marroquin, F. Advanced electrochemical energy storage supercapacitors based on the flexible carbon fiber fabric-coated with uni-

form coral-like MnO2 structured electrodes. *Chemical Engineering Journal* **2017**, *309*, 151–158.

(19) Liu, Z.; Robinson, J. T.; Sun, X.; Dai, H. PEGylated nanographene oxide for delivery of water-insoluble cancer drugs. *Journal of the American Chemical Society* **2008**, *130*, 10876–10877.

(20) Liu, J.; Xue, Y.; Gao, Y.; Yu, D.; Durstock, M.; Dai, L. Hole and electron extraction layers based on graphene oxide derivatives for high-performance bulk heterojunction solar cells. *Advanced Materials* **2012**, *24*, 2228–2233.

(21) Han, T.-H.; Lee, Y.; Choi, M.-R.; Woo, S.-H.; Bae, S.-H.; Hong, B. H.; Ahn, J.-H.; Lee, T.-W. Extremely efficient flexible organic light-emitting diodes with modified graphene anode. *Nature Photonics* **2012**, *6*, 105–110.

(22) Loh, K. P.; Bao, Q.; Eda, G.; Chhowalla, M. Graphene oxide as a chemically tunable platform for optical applications. *Nature Chemistry 2010 2:12* **2010**, *2*, 1015–1024.

(23) Mak, K. F.; Lee, C.; Hone, J.; Shan, J.; Heinz, T. F. Atomically thin MoS2: A new direct-gap semiconductor. *Physical Review Letters* **2010**, *105*, 2–5.

(24) Chhowalla, M.; Shin, H. S.; Eda, G.; Li, L. J.; Loh, K. P.; Zhang, H. The chemistry of two-dimensional layered transition metal dichalcogenide nanosheets. *Nature Chemistry* **2013**, *5*, 263–275.

(25) Wang, Q. H.; Kalantar-Zadeh, K.; Kis, A.; Coleman, J. N.; Strano, M. S. Electronics and optoelectronics of two-dimensional transition metal dichalcogenides. *Nature Nanotechnology* **2012**, *7*, 699–712.

(26) Georgiou, T.; Jalil, R.; Belle, B. D.; Britnell, L.; Gorbachev, V. R.; Morozov, V. S.; Kim, Y. J.; Gholinia, A.; Haigh, S. J.; Makarovsky, O.; Eaves, L.; Ponomarenko, L. A.; Geim, A. K.; Novoselov, K. S.; Mishchenko, A. Vertical field-effect transistor based on graphene-WS 2 heterostructures for flexible and transparent electronics. *Nature Nanotechnology* **2013**, *8*, 100–103.

(27) Åđahin, H.; Cahangirov, S.; Topsakal, M.; Bekaroglu, E.; Akturk, E.; Senger, R. T.; Ciraci, S. Monolayer honeycomb structures of group-IV elements and III-V binary compounds: First-principles calculations. *Physical Review B - Condensed Matter and Materials Physics* **2009**, *80*, 1–12.

(28) Molle, A.; Goldberger, J.; Houssa, M.; Xu, Y.; Zhang, S. C.; Akinwande, D. Buckled two-dimensional Xene sheets. *Nature Materials* **2017**, *16*, 163–169.

(29) Matthes, L.; Pulci, O.; Bechstedt, F. Optical properties of two-dimensional honeycomb crystals graphene, silicene, germanene, and tinene from first principles. *New Journal of Physics* **2014**, *16*.

(30) Watanabe, K.; Taniguchi, T.; Kanda, H. Direct-bandgap properties and evidence for ultraviolet lasing of hexagonal boron nitride single crystal. *Nature Materials 2004 3:6* **2004**, *3*, 404–409.

(31) Beal, A.; Hughes, H.; Liang, W. The reflectivity spectra of some group VA transition metal dichalcogenides. *Journal of physics C: solid state physics* **1975**, *8*, 4236.

(32) Ataca, C.; Sahin, H.; Ciraci, S. Stable, single-layer MX2 transition-metal oxides and dichalcogenides in a honeycomb-like structure. *The Journal of Physical Chemistry C* **2012**, *116*, 8983–8999.

(33) Wilson, J. A.; Di Salvo, F.; Mahajan, S. Charge-density waves and superlattices in the metallic layered transition metal dichalcogenides. *Advances in Physics* **1975**, *24*, 117–201.

(34) Liu, L.; Kumar, S. B.; Ouyang, Y.; Guo, J. Performance limits of monolayer transition metal dichalcogenide transistors. *IEEE Transactions on Electron Devices* **2011**, *58*, 3042–3047.

(35) Kuc, A.; Zibouche, N.; Heine, T. Influence of quantum confinement on the electronic structure of the transition metal sulfide T S 2. *Physical Review B* **2011**, *83*, 245213.

(36) Kam, K.; Parkinson, B. Detailed photocurrent spectroscopy of the semiconducting group VIB transition metal dichalcogenides. *The Journal of Physical Chemistry* **1982**, *86*, 463–467.

(37) Liu, T.; Wang, C.; Cui, W.; Gong, H.; Liang, C.; Shi, X.; Li, Z.; Sun, B.; Liu, Z. Combined photothermal and photodynamic therapy delivered by PEGylated MoS2 nanosheets. *Nanoscale* **2014**, *6*, 11219–11225.

(38) Voiry, D.; Yang, J.; Chhowalla, M. Recent strategies for improving the catalytic activity of 2D TMD nanosheets toward the hydrogen evolution reaction. *Advanced materials* **2016**, *28*, 6197–6206.

(39) Bernardi, M.; Palummo, M.; Grossman, J. C. Extraordinary sunlight absorption and one nanometer thick photovoltaics using two-dimensional monolayer materials. *Nano letters* **2013**, *13*, 3664–3670.

(40) Chou, S. S.; Kaehr, B.; Kim, J.; Foley, B. M.; De, M.; Hopkins, P. E.; Huang, J.; Brinker, C. J.; Dravid, V. P. Chemically exfoliated MoS2 as near-infrared photothermal agents. *Angewandte Chemie International Edition* **2013**, *52*, 4160–4164.

(41) Dong, H.; Tang, S.; Hao, Y.; Yu, H.; Dai, W.; Zhao, G.; Cao, Y.; Lu, H.; Zhang, X.; Ju, H. Fluorescent MoS2 quantum dots: ultrasonic preparation, up-conversion and down-conversion bioimaging, and photodynamic therapy. *ACS applied materials & interfaces* **2016**, *8*, 3107–3114.

(42) Wang, T.; Zhu, H.; Zhuo, J.; Zhu, Z.; Papakonstantinou, P.; Lubarsky, G.; Lin, J.; Li, M. Biosensor based on ultrasmall MoS2 nanoparticles for electrochemical detection of H2O2 released by cells at the nanomolar level. *Analytical chemistry* **2013**, *85*, 10289–10295.

(43) Roy, S.; Bobde, Y.; Ghosh, B.; Chakraborty, C. Targeted Bioimaging of Cancer Cells Using Free Folic Acid-Sensitive Molybdenum Disulfide Quantum Dots through Fluorescence âĂIJTurn-OffâĂİ. *ACS Applied Bio Materials* **2021**, *4*, 2839–2849.

(44) Sivadas, N.; Daniels, M. W.; Swendsen, R. H.; Okamoto, S.; Xiao, D. Magnetic ground state of semiconducting transition-metal trichalcogenide monolayers. *Phys. Rev. B* **2015**, *91*, 235425.

(45) LÃl'vy, F.; Berger, H. Single crystals of transition metal trichalcogenides. *Journal of Crystal Growth* **1983**, *61*, 61–68.

(46) Dai, J.; Li, M.; Zeng, X. C. Group IVB transition metal trichalcogenides: a new class of 2D layered materials beyond graphene. *WIREs Computational Molecular Science* **2016**, *6*, 211–222.

(47) John, T. T.; Bini, S.; Kashiwaba, Y.; Abe, T.; Yasuhiro, Y.; Kartha, C. S.; Vijayakumar, K. P. Characterization of spray pyrolysed indium sulfide thin films. *Semiconductor Science and Technology* **2003**, *18*, 491–500.

(48) Li, L.; Pandey, A.; Werder, D. J.; Khanal, B. P.; Pietryga, J. M.; Klimov, V. I. Efficient synthesis of highly luminescent copper indium sulfide-based core/shell nanocrystals with surprisingly long-lived emission. *Journal of the American Chemical Society* **2011**, *133*, 1176–1179.

(49) Barreau, N. Indium sulfide and relatives in the world of photovoltaics. *Solar Energy* **2009**, *83*, 363–371.

(50) Hu, P.; Wen, Z.; Wang, L.; Tan, P.; Xiao, K. Synthesis of few-layer GaSe nanosheets for high performance photodetectors. *ACS nano* **2012**, *6*, 5988–5994.

(51) Vaughn, D. D.; Patel, R. J.; Hickner, M. A.; Schaak, R. E. Single-crystal colloidal nanosheets of GeS and GeSe. *Journal of the American Chemical Society* **2010**, *132*, 15170–15172.

(52) Lei, S.; Ge, L.; Liu, Z.; Najmaei, S.; Shi, G.; You, G.; Lou, J.; Vajtai, R.; Ajayan, P. M. Synthesis and photoresponse of large GaSe atomic layers. *Nano letters* **2013**, *13*, 2777–2781.

(53) Late, D. J.; Liu, B.; Luo, J.; Yan, A.; Matte, H. S. S. R.; Grayson, M.; Rao, C. N. R.; Dravid, V. P. GaS and GaSe Ultrathin Layer Transistors. *Advanced Materials* **2012**, *24*, 3549–3554.

(54) Fei, R.; Li, W.; Li, J.; Yang, L. Giant piezoelectricity of monolayer group IV monochalcogenides. APS March Meeting Abstracts. 2016; pp F15–008.

(55) Geim, A. K.; Grigorieva, I. V. Van der Waals heterostructures. *Nature* **2013**, *499*, 419–425.

(56) Ponomarenko, L.; Geim, A.; Zhukov, A.; Jalil, R.; Morozov, S.; Novoselov, K.; Grigorieva, I.; Hill, E.; Cheianov, V.; FalâĂŹKo, V.; Watanabe, K.; Taniguchi, T.; Gorbachev, R. V. Tunable metal–insulator transition in double-layer graphene heterostructures. *Nature Physics* **2011**, *7*, 958–961.

(57) Haigh, S.; Gholinia, A.; Jalil, R.; Romani, S.; Britnell, L.; Elias, D.; Novoselov, K.; Ponomarenko, L.; Geim, A.; Gorbachev, R. Cross-sectional imaging of individual layers and buried interfaces of graphene-based heterostructures and superlattices. *Nature materials* **2012**, *11*, 764–767.

(58) Dean, C.; Young, A.; Wang, L.; Meric, I.; Lee, G.-H.; Watanabe, K.; Taniguchi, T.; Shepard, K.; Kim, P.; Hone, J. Graphene based heterostructures. *Solid State Communications* **2012**, *152*, 1275–1282.

(59) Gorbachev, R.; Geim, A.; Katsnelson, M.; Novoselov, K.; Tudorovskiy, T.; Grigorieva, I.; MacDonald, A.; Morozov, S.; Watanabe, K.; Taniguchi, T.; Ponomarenko, L. Strong Coulomb drag and broken symmetry in double-layer graphene. *Nature Physics* **2012**, *8*, 896–901.

(60) Georgiou, T.; Jalil, R.; Belle, B. D.; Britnell, L.; Gorbachev, R. V.; Morozov, S. V.; Kim, Y.-J.; Gholinia, A.; Haigh, S. J.; Makarovsky, O.; Eaves, L.; Ponomarenko, L. A.; Geim, A. K.; Novoselov, K. J.; Mishchenko, A. Vertical field-effect transistor based on graphene–WS_2 heterostructures for flexible and transparent electronics. *Nature nanotechnology* **2013**, *8*, 100–103.

(61) Gong, Y.; Lei, S.; Ye, G.; Li, B.; He, Y.; Keyshar, K.; Zhang, X.; Wang, Q.; Lou, J.; Liu, Z.; Vajtai, R.; Zhou, W.; Ajayan, P. M. Two-step growth of two-dimensional WSe_2/$MoSe_2$ heterostructures. *Nano letters* **2015**, *15*, 6135–6141.

(62) Jin, H.; Li, J.; Wang, B.; Yu, Y.; Wan, L.; Xu, F.; Dai, Y.; Wei, Y.; Guo, H. Electronics and optoelectronics of lateral heterostructures within monolayer indium monochalcogenides. *Journal of Materials Chemistry C* **2016**, *4*, 11253–11260.

(63) Yagmurcukardes, M.; Torun, E.; Senger, R. T.; Peeters, F. M.; Sahin, H. Mg (OH) 2- WS 2 van der Waals heterobilayer: Electric field tunable band-gap crossover. *Physical Review B* **2016**, *94*, 195403.

(64) Rivera, P.; Schaibley, J. R.; Jones, A. M.; Ross, J. S.; Wu, S.; Aivazian, G.; Klement, P.; Seyler, K.; Clark, G.; Ghimire, N. J.; Yan, J.; Mandrus, D.; Yao, W.; Xu, X. Observation of long-lived interlayer excitons in monolayer $MoSe_2$–WSe_2 heterostructures. *Nature communications* **2015**, *6*, 1–6.

(65) Tang, H.-L.; Chiu, M.-H.; Tseng, C.-C.; Yang, S.-H.; Hou, K.-J.; Wei, S.-Y.; Huang, J.-K.; Lin, Y.-F.; Lien, C.-H.; Li, L.-J. Multilayer graphene–WSe2 heterostructures for WSe_2 transistors. *ACS nano* **2017**, *11*, 12817–12823.

(66) Qiao, H.; Yuan, J.; Xu, Z.; Chen, C.; Lin, S.; Wang, Y.; Song, J.; Liu, Y.; Khan, Q.; Hoh, H. Y.; Pan, C.-X.; Li, S. Broadband photodetectors based on graphene–Bi_2Te_3 heterostructure. *Acs Nano* **2015**, *9*, 1886–1894.

(67) Hohenberg, P.; Kohn, W. Inhomogeneous electron gas. *Phys. Rev.* **1964**, *136*, B864.

(68) Kohn, W.; Sham, L. J. Self-consistent equations including exchange and correlation effects. *Phys. Rev.* **1965**, *140*, A1133.

(69) Hellmann, H. Einfuhrung in die quantumchemie (leipzig: Franz deutsche 1937). *Phys. Rev.* **1939**, *56*, 340.

(70) Feynman, R. P. Forces in molecules. *Phys. Rev.* **1939**, *56*, 340–343.

(71) Adamo, C.; Barone, V. Toward reliable density functional methods without adjustable parameters: The PBE0 model. *J. Chem. Phys.* **1999**, *110*, 6158–6170.

(72) Ernzerhof, M.; Scuseria, G. E. Assessment of the Perdew–Burke–Ernzerhof exchange-correlation functional. *J. Chem. Phys.* **1999**, *110*, 5029–5036.

(73) Becke, A. D. Density-functional exchange-energy approximation with correct asymptotic behavior. *Phys. Rev. A* **1988**, *38*, 3098–3100.

(74) Lee, C.; Yang, W.; Parr, R. G. Development of the Colle-Salvetti correlation-energy formula into a functional of the electron density. *Phys. Rev. B* **1988**, *37*, 785–789.

(75) Axel, D. B. Density-functional thermochemistry. III. The role of exact exchange. *J. Chem. Phys.* **1993**, *98*, 5648–5652.

(76) Heyd, J.; Scuseria, G. E.; Ernzerhof, M. Hybrid functionals based on a screened Coulomb potential. *J. Chem. Phys.* **2003**, *118*, 8207–8215.

(77) Heyd, J.; Scuseria, G. E. Efficient hybrid density functional calculations in solids: Assessment of the Heyd-Scuseria-Ernzerhof screened Coulomb hybrid functional. *J. Chem. Phys.* **2004**, *121*, 1187–1192.

(78) Krukau, A. V.; Vydrov, O. A.; Izmaylov, A. F.; Scuseria, G. E. Influence of the exchange screening parameter on the performance of screened hybrid functionals. *J. Chem. Phys.* **2006**, *125*, 224106.

(79) Kresse, G.; Hafner, J. Ab initio molecular dynamics for liquid metals. *Physical Review B* **1993**, *47*, 558.

(80) Kresse, G.; Furthmüller, J. Efficient iterative schemes for ab initio total-energy calculations using a plane-wave basis set. *Physical review B* **1996**, *54*, 11169.

(81) Perdew, J. P.; Burke, K.; Ernzerhof, M. Generalized gradient approximation made simple. *Physical review letters* **1996**, *77*, 3865.

(82) Grimme, S.; Ehrlich, S.; Goerigk, L. Effect of the damping function in dispersion corrected density functional theory. *Journal of computational chemistry* **2011**, *32*, 1456–1465.

(83) Ge, H. J. S.; Ernzerhof, M. Erratum:âĂIJHybrid functionals based on a screened Coulomb potentialâĂİ[J. Chem. Phys. 118, 8207 (2003)]. *J Chem Phys* **2006**, *124*, 219906.

(84) Kresse, G.; Joubert, D. From ultrasoft pseudopotentials to the projector augmented-wave method. *Phys. Rev. B* **1999**, *59*, 1758–1775.

(85) Blöchl, P. E. Projector augmented-wave method. *Phys. Rev. B* **1994**, *50*, 17953.

(86) Kresse, G.; Hafner, J. Ab initio molecular dynamics for liquid metals. *Phys. Rev. B* **1993**, *47*, 558.

(87) Kresse, G.; Furthmüller, J. Efficient iterative schemes for ab initio total-energy calculations using a plane-wave basis set. *Phys. Rev. B* **1996**, *54*, 11169–11186.

(88) Perdew, J. P.; Burke, K.; Ernzerhof, M. Generalized gradient approximation made simple. *Phys. Rev. Lett.* **1996**, *77*, 3865–3868.

(89) Henkelman, G.; Arnaldsson, A.; Jónsson, H. A fast and robust algorithm for Bader decomposition of charge density. *Comput. Mater. Sci.* **2006**, *36*, 354–360.

(90) Togo, A.; Oba, F.; Tanaka, I. First-principles calculations of the ferroelastic transition between rutile-type and $CaCl_2$-type SiO_2 at high pressures. *Phys. Rev. B* **2008**, *78*, 134106.

(91) Alfè, D. PHON: A program to calculate phonons using the small displacement method. *Comput. Phys. Commun.* **2009**, *180*, 2622–2633.

(92) Grimme, S. Semiempirical GGA-type density functional constructed with a long-range dispersion correction. *J. Comput. Chem.* **2006**, *27*, 1787–1799.

(93) Grimme, S.; Ehrlich, S.; Goerigk, L. Effect of the damping function in dispersion corrected density functional theory. *J. Comput. Chem.* **2011**, *32*, 1456–1465.

(94) Adachi, S. GaAs, AlAs, and Al x Ga1- x As: Material parameters for use in research and device applications. *Journal of Applied Physics* **1985**, *58*, R1–R29.

(95) Martienssen, W.; Warlimont, H. *Springer handbook of condensed matter and materials data*; Springer Science & Business Media, 2006.

(96) Vurgaftman, I.; Meyer, J. á.; Ram-Mohan, L. á. Band parameters for III–V compound semiconductors and their alloys. *Journal of applied physics* **2001**, *89*, 5815–5875.

(97) Nakamura, S.; Senoh, M.; Nagahama, S.-i.; Iwasa, N.; Yamada, T.; Matsushita, T.; Kiyoku, H.; Sugimoto, Y. InGaN-based multi-quantum-well-structure laser diodes. *Japanese Journal of Applied Physics* **1996**, *35*, L74.

(98) Liu, H.; Wang, T.; Jiang, Q.; Hogg, R.; Tutu, F.; Pozzi, F.; Seeds, A. Long-wavelength InAs/GaAs quantum-dot laser diode monolithically grown on Ge substrate. *Nature Photonics* **2011**, *5*, 416–419.

(99) Halioua, Y.; Bazin, A.; Monnier, P.; Karle, T.; Roelkens, G.; Sagnes, I.; Raj, R.; Raineri, F. Hybrid III-V semiconductor/silicon nanolaser. *Optics express* **2011**, *19*, 9221–9231.

(100) Yamaguchi, M. Fundamentals and R&D status of III-V compound solar cells and materials. *physica status solidi (c)* **2015**, *12*, 489–499.

(101) Lee, K.-H.; Araki, K.; Wang, L.; Kojima, N.; Ohshita, Y.; Yamaguchi, M. Assessing material qualities and efficiency limits of III–V on silicon solar cells using external radiative efficiency. *Progress in Photovoltaics: Research and Applications* **2016**, *24*, 1310–1318.

(102) Krames, M. R.; Shchekin, O. B.; Mueller-Mach, R.; Mueller, G. O.; Zhou, L.; Harbers, G.; Craford, M. G. Status and future of high-power light-emitting diodes for

solid-state lighting. *Journal of display technology* **2007**, *3*, 160–175.

(103) Taniyasu, Y.; Kasu, M.; Makimoto, T. An aluminium nitride light-emitting diode with a wavelength of 210 nanometres. *nature* **2006**, *441*, 325–328.

(104) Roest, A. L.; Verheijen, M. A.; Wunnicke, O.; Serafin, S.; Wondergem, H.; Bakkers, E. P. Position-controlled epitaxial III–V nanowires on silicon. *Nanotechnology* **2006**, *17*, S271.

(105) Zhang, Y.; Wu, J.; Aagesen, M.; Liu, H. III–V nanowires and nanowire optoelectronic devices. *Journal of Physics D: Applied Physics* **2015**, *48*, 463001.

(106) Birowosuto, M. D.; Yokoo, A.; Zhang, G.; Tateno, K.; Kuramochi, E.; Taniyama, H.; Takiguchi, M.; Notomi, M. Movable high-Q nanoresonators realized by semiconductor nanowires on a Si photonic crystal platform. *Nature Materials* **2014**, *13*, 279–285.

(107) Norouzzadeh, P.; Shakouri, A.; Vashaee, D. Valleytronics of III–V solid solutions for thermoelectric application. *RSC advances* **2017**, *7*, 7310–7314.

(108) Zhu, C.; Yang, R.; Wei, Q.; Zhang, D. Theoretical investigations of phases of AlAs by first-principles. *Chinese journal of physics* **2018**, *56*, 2119–2128.

(109) Liu, C.; Ma, M.; Yuan, X.; Sun, H.; Ying, P.; Xu, B.; Zhao, Z.; He, J. Metastable phases, phase transformation and properties of AlAs based on first-principle study. *Computational Materials Science* **2017**, *128*, 337–342.

(110) Guo, L. Structural, energetic, and electronic properties of hydrogenated aluminum arsenide clusters. *Journal of Nanoparticle Research* **2011**, *13*, 2029–2039.

(111) Yan, J.; Ke, F.; Liu, C.; Wang, Q.; Zhang, J.; Wang, L.; Peng, G.; Han, Y.; Ma, Y.; Gao, C. Electrical transport properties of AlAs under compression: reversible boundary effect. *Physical Chemistry Chemical Physics* **2015**, *17*, 26277–26282.

(112) Cao, J.; Huang, M.; Liu, D.; Cai, Z.; Wu, Y.-N.; Ye, X.; Chen, S. Defects and dopants in zinc-blende aluminum arsenide: a first-principles study. *New Journal of Physics* **2021**, *23*, 013018.

(113) De Poortere, E.; Shkolnikov, Y.; Shayegan, M. High-mobility electrons in modulation-doped AlAs quantum wells. *Physica E: Low-dimensional Systems and Nanostructures* **2002**, *13*, 646–648.

(114) Rami, R.; Drissi, L.; Rkhioui, N.; Drissi El Bouzaidi, M.; Ahl Laamara, R. (V, Ti) co-doping effect on electronic and magnetic properties of zb-AlAs. *International Journal of Modern Physics B* **2019**, *33*, 1950326.

(115) Mitchell, W.; Chung, C.-H.; Yi, S.; Hu, E.; Weinberg, W. Oxidation of AlAs films under ultrahigh vacuum conditions: interaction of H2O and O2 with the AlAs (001) surface. *Surface science* **1997**, *384*, 81–93.

(116) Moser, J.; Zibold, T.; Schuh, D.; Bichler, M.; Ertl, F.; Abstreiter, G.; Grayson, M.; Roddaro, S.; Pellegrini, V. Aluminum arsenide cleaved-edge overgrown quantum wires. *Applied Physics Letters* **2005**, *87*, 052101.

(117) Merlin, R.; Bajema, K.; Clarke, R.; Juang, F.-Y.; Bhattacharya, P. Quasiperiodic gaas-alas heterostructures. *Physical review letters* **1985**, *55*, 1768.

(118) Sakaki, H.; Noda, T.; Hirakawa, K.; Tanaka, M.; Matsusue, T. Interface roughness scattering in GaAs/AlAs quantum wells. *Applied physics letters* **1987**, *51*, 1934–1936.

(119) Laidig, W.; Holonyak Jr, N.; Camras, M.; Hess, K.; Coleman, J.; Dapkus, P.; Bardeen, J. Disorder of an AlAs-GaAs superlattice by impurity diffusion. *Applied Physics Letters* **1981**, *38*, 776–778.

(120) Pogrel, M. A.; Chen, J. W.; Zhang, K. Effects of low-energy gallium-aluminum-arsenide laser irradiation on cultured fibroblasts and keratinocytes. *Lasers in Surgery and Medicine: The Official Journal of the American Society for Laser*

Medicine and Surgery **1997**, *20*, 426–432.

(121) Hagiwara, S.; Iwasaka, H.; Hasegawa, A.; Noguchi, T. Pre-irradiation of blood by gallium aluminum arsenide (830 nm) low-level laser enhances peripheral endogenous opioid analgesia in rats. *Anesthesia & Analgesia* **2008**, *107*, 1058–1063.

(122) Sood, A.; Menendez, J.; Cardona, M.; Ploog, K. Interface vibrational modes in GaAs-AlAs superlattices. *Physical review letters* **1985**, *54*, 2115.

(123) Yu, X.; Chen, G.; Verma, A.; Smith, J. Temperature dependence of thermophysical properties of GaAs/AlAs periodic structure. *Applied Physics Letters* **1995**, *67*, 3554–3556.

(124) Capinski, W. S.; Maris, H. J. Thermal conductivity of GaAs/AlAs superlattices. *Physica B: Condensed Matter* **1996**, *219*, 699–701.

(125) Mendez, E.; Wang, W.; Ricco, B.; Esaki, L. Resonant tunneling of holes in AlAs-GaAs-AlAs heterostructures. *Applied physics letters* **1985**, *47*, 415–417.

(126) Brotons-Gisbert, M.; Andres-Penares, D.; Suh, J.; Hidalgo, F.; Abargues, R.; Rodriguez-Canto, P. J.; Segura, A.; Cros, A.; Tobias, G.; Canadell, E.; Ordejón, P.; Wu, J.; Martínez-Pastor, J. P.; Sánchez-Royo, J. F. Nanotexturing to enhance photoluminescent response of atomically thin indium selenide with highly tunable band gap. *Nano letters* **2016**, *16*, 3221–3229.

(127) Bandurin, D. A. et al. High electron mobility, quantum Hall effect and anomalous optical response in atomically thin InSe. *Nature nanotechnology* **2017**, *12*, 223–227.

(128) Lei, S.; Wen, F.; Ge, L.; Najmaei, S.; George, A.; Gong, Y.; Gao, W.; Jin, Z.; Li, B.; Lou, J.; Kono, J.; Vajtai, R.; Ajayan, P.; Halas, N. J. An atomically layered InSe avalanche photodetector. *Nano letters* **2015**, *15*, 3048–3055.

(129) Yang, Z.; Jie, W.; Mak, C.-H.; Lin, S.; Lin, H.; Yang, X.; Yan, F.; Lau, S. P.; Hao, J.

Wafer-scale synthesis of high-quality semiconducting two-dimensional layered InSe with broadband photoresponse. *ACS nano* **2017**, *11*, 4225–4236.

(130) Hu, T.; Zhou, J.; Dong, J. Strain induced new phase and indirect–direct band gap transition of monolayer InSe. *Physical Chemistry Chemical Physics* **2017**, *19*, 21722–21728.

(131) Jin, H.; Li, J.; Dai, Y.; Wei, Y. Engineering the electronic and optoelectronic properties of InX (X= S, Se, Te) monolayers via strain. *Physical Chemistry Chemical Physics* **2017**, *19*, 4855–4860.

(132) Cai, Y.; Zhang, G.; Zhang, Y.-W. Charge transfer and functionalization of monolayer InSe by physisorption of small molecules for gas sensing. *The Journal of Physical Chemistry C* **2017**, *121*, 10182–10193.

(133) Qin, L.; Zhang, Z.-H.; Jiang, Z.; Fan, K.; Zhang, W.-H.; Tang, Q.-Y.; Xia, H.-N.; Meng, F.; Zhang, Q.; Gu, L.; West, D.; Zhang, S.; Fu, Y.-S. Realization of AlSb in the Double-Layer Honeycomb Structure: A Robust Class of Two-Dimensional Material. *ACS nano* **2021**, *15*, 8184–8191.

(134) Hamer, M. J. et al. Indirect to direct gap crossover in two-dimensional InSe revealed by angle-resolved photoemission spectroscopy. *ACS nano* **2019**, *13*, 2136–2142.

(135) Johnson, W. C. Nitrogen compounds of germanium. I. The preparation and properties of Germanic nitride. *J. Am. Chem. Soc* **1930**, *52*, 5160–5165.

(136) He, H.; Sekine, T.; Kobayashi, T.; Kimoto, K. Phase transformation of germanium nitride (Ge_3N_4) under shock wave compression. *J. Appl. Phys* **2001**, *90*, 4403–4406.

(137) Serghiou, G.; Miehe, G.; Tschauner, O.; Zerr, A.; Boehler, R. Synthesis of a cubic Ge_3N_4 phase at high pressures and temperatures. *J. Chem. Phys* **1999**, *111*, 4659–4662.

(138) Leinenweber, K.; O'keeffe, M.; Somayazulu, M.; Hubert, H.; McMillan, P.; Wolf, G. Synthesis and structure refinement of the spinel, γ-Ge_3N_4. *Chem-Eur. J* **1999**, *5*, 3076–3078.

(139) Maeda, T.; Yasuda, T.; Nishizawa, M.; Miyata, N.; Morita, Y.; Takagi, S. Pure germanium nitride formation by atomic nitrogen radicals for application to Ge metal-insulator-semiconductor structures. *J. Appl. Phys* **2006**, *100*, 014101.

(140) Nishiyama, N.; Langer, J.; Sakai, T.; Kojima, Y.; Holzheid, A.; Gaida, N. A.; Kulik, E.; Hirao, N.; Kawaguchi, S. I.; Irifune, T. Phase relations in silicon and germanium nitrides up to 98 GPa and 2400Âř C. *J. Am. Ceram. Soc* **2019**, *102*, 2195–2202.

(141) Molina, B.; Sansores, L. Electronic structure of Ge_3N_4 possible structures. *Int. J. Quantum Chem* **2000**, *80*, 249–257.

(142) Sevik, C.; Bulutay, C. Theoretical study of the insulating oxides and nitrides: SiO_2, GeO_2, Al_2O_3, Si_3N_4, and Ge_3N_4. *J. Mater. Sci* **2007**, *42*, 6555–6565.

(143) Chu, I.-H.; Kozhevnikov, A.; Schulthess, T. C.; Cheng, H.-P. All-electron GW quasiparticle band structures of group 14 nitride compounds. *J. Chem. Phys* **2014**, *141*, 044709.

(144) Gao, S.-P.; Cai, G.; Xu, Y. Band structures for Ge_3N_4 polymorphs studied by DFT-LDA and GWA. *Comp. Mater. Sci* **2013**, *67*, 292–295.

(145) Boyko, T.; Hunt, A.; Zerr, A.; Moewes, A. Electronic structure of spinel-type nitride compounds Si_3N_4, Ge_3N_4, and Sn_3N_4 with tunable band gaps: application to light emitting diodes. *Phys. Rev. Lett* **2013**, *111*, 097402.

(146) Jayatunga, B. H. D.; Lambrecht, W. R. Quasiparticle self-consistent G W energy band calculations for Ge_3N_4 phases. *Phys. Rev. B* **2020**, *102*, 195203.

(147) Xiang, H.; Feng, Z.; Li, Z.; Zhou, Y. Theoretical predicted high-thermal-conductivity cubic Si_3N_4 and Ge_3N_4: promising substrate materials for high-power electronic

devices. *Sci. Rep-UK* **2018**, *8*, 1–9.

(148) Caskey, C. M.; Seabold, J. A.; Stevanović, V.; Ma, M.; Smith, W. A.; Ginley, D. S.; Neale, N. R.; Richards, R. M.; Lany, S.; Zakutayev, A. Semiconducting properties of spinel tin nitride and other IV_3 N_4 polymorphs. *J. Mater. Chem. C* **2015**, *3*, 1389–1396.

(149) Maeda, T.; Yasuda, T.; Nishizawa, M.; Miyata, N.; Morita, Y.; Takagi, S. Ge metal-insulator-semiconductor structures with Ge_3N_4 dielectrics by direct nitridation of Ge substrates. *Appl. Phys. Lett* **2004**, *85*, 3181–3183.

(150) Okamoto, G.; Kutsuki, K.; Hosoi, T.; Shimura, T.; Watanabe, H. Electrical characteristics of Ge-based metal-insulator-semiconductor devices with Ge_3N_4 dielectrics formed by plasma nitridation. *J. Nanosci. Nanotechno* **2011**, *11*, 2856–2860.

(151) Lucovsky, G.; Lee, S.; Long, J.; Seo, H.; Lüning, J. Elimination of GeO_4 and Ge_3N_4 interfacial transition regions and defects at n-type Ge interfaces: A pathway for formation of n-MOS devices on Ge substrates. *App. Surf. Sci* **2008**, *254*, 7933–7937.

(152) Lieten, R.; AfanasâĂŹev, V.; Thoan, N.; Degroote, S.; Walukiewicz, W.; Borghs, G. Mechanisms of Schottky barrier control on n-type germanium using Ge_3N_4 interlayers. *J. Electrochem. Soc* **2011**, *158*, H358.

(153) Ma, Y.; Wang, M.; Zhou, X. First-principles investigation of β-Ge_3N_4 loaded with RuO_2 cocatalyst for photocatalytic overall water splitting. *J. Energy Chem* **2020**, *44*, 24–32.

(154) Lee, Y.; Watanabe, T.; Takata, T.; Hara, M.; Yoshimura, M.; Domen, K. Effect of high-pressure ammonia treatment on the activity of Ge_3N_4 photocatalyst for overall water splitting. *The J. Phys. Chem. B* **2006**, *110*, 17563–17569.

(155) Sánchez-Palencia, P.; García, G.; Conesa, J. C.; Wahnón, P.; Palacios, P. Spinel-Type nitride compounds with improved features as solar cell absorbers. *Acta Mater*

2020, *197*, 316–329.

(156) Sahin, H.; Cahangirov, S.; Topsakal, M.; Bekaroglu, E.; Akturk, E.; Senger, R. T.; Ciraci, S. Monolayer honeycomb structures of group-IV elements and III-V binary compounds: First-principles calculations. *Phys. Rev. B* **2009**, *80*, 155453.

(157) Yagmurcukardes, M.; Senger, R.; Peeters, F.; Sahin, H. Mechanical properties of monolayer GaS and GaSe crystals. *Phys. Rev. B* **2016**, *94*, 245407.

(158) Lee, C.; Wei, X.; Kysar, J. W.; Hone, J. Measurement of the elastic properties and intrinsic strength of monolayer graphene. *science* **2008**, *321*, 385–388.

(159) Chen, B.; Sahin, H.; Suslu, A.; Ding, L.; Bertoni, M. I.; Peeters, F.; Tongay, S. Environmental changes in $MoTe_2$ excitonic dynamics by defects-activated molecular interaction. *Acs Nano* **2015**, *9*, 5326–5332.

(160) Li, L. H.; Chen, Y. Atomically thin boron nitride: unique properties and applications. *Advanced Functional Materials* **2016**, *26*, 2594–2608.

(161) Yagmurcukardes, M.; Bacaksiz, C.; Unsal, E.; Akbali, B.; Senger, R.; Sahin, H. Strain mapping in single-layer two-dimensional crystals via Raman activity. *Phys. Rev. B* **2018**, *97*, 115427.

(162) Torun, E.; Sahin, H.; Cahangirov, S.; Rubio, A.; Peeters, F. Anisotropic electronic, mechanical, and optical properties of monolayer WTe_2. *J. Appl. Phys* **2016**, *119*, 074307.